NeuroImage 259 (2022) 119401

Contents lists available at ScienceDirect

NeuroImage

journal homepage: www.elsevier.com/locate/neuroimage

Cross-attractor repertoire provides new perspective on structure-function relationship in the brain

Mengsen Zhang [a,b,*], Yinming Sun [a], Manish Saggar [a,*]

[a] Department of Psychiatry and Behavioral Sciences, Stanford University, Stanford, CA 94304, USA
[b] Department of Psychiatry, University of North Carolina at Chapel Hill, Chapel Hill, NC 27514, USA

A B S T R A C T

The brain exhibits complex intrinsic dynamics, i.e., spontaneously arising activity patterns without any external inputs or tasks. Such intrinsic dynamics and their alteration are thought to play crucial roles in typical as well as atypical cognitive functioning. Linking the ever-changing intrinsic dynamics to the rather static anatomy is a challenging endeavor. Dynamical systems models are important tools for understanding how structure and function are linked in the brain. Here, we provide a novel modeling framework to examine how functional connectivity depends on structural connectivity in the brain. Existing modeling frameworks typically focus on noise-driven (or stochastic) dynamics near a single attractor. Complementing existing approaches, we examine deterministic features of the distribution of attractors, in particular, how regional states are correlated across all attractors – cross-attractor coordination. We found that cross-attractor coordination between brain regions better predicts human functional connectivity than noise-driven single-attractor dynamics. Importantly, cross-attractor coordination better accounts for the nonlinear dependency of functional connectivity on structural connectivity. Our findings suggest that functional connectivity patterns in the brain may reflect transitions between attractors, which impose an energy cost. The framework may be used to predict transitions and energy costs associated with experimental or clinical interventions.

1. Introduction

A fundamental goal of neuroscience is to understand how the structure of the brain constrains its function (Sporns and Tononi, 2001). The advent of neuroimaging techniques has enabled detailed, quantitative examination of the structure-function relation, often by comparing the structural and functional connectivity between brain regions (Damoiseaux and Greicius, 2009; van den Heuvel and Pol, 2010). The resting-state functional connectivity is of particular interest, given its relevance to a variety of cognitive functions, neurological diseases, and psychiatric disorders (van den Heuvel and Pol, 2010; Saggar and Uddin, 2019). Though structural connectivity and functional connectivity are correlated, the former does not entirely predict the latter—strong functional coupling exists between regions with only weak or indirect structural connections (Damoiseaux and Greicius, 2009; Honey et al., 2009). Nonlinear dynamical models have been used to provide a mechanistic understanding of the structure-function relation (Breakspear, 2017; Deco et al., 2011; Park and Friston, 2013) and provided many insights (e.g. Deco et al. (2009, 2014, 2013b); Demirta et al. (2019); Ghosh et al. (2008); Golos et al. (2015); Hansen et al. (2015); Honey et al. (2007)). While successful, previous dynamical system approaches often focus on dynamics near a single stable state, i.e., an attractor. However, biological systems such as the brain are often multistable (Kelso, 2012; Laurent and Kellershohn, 1999; Zhang et al., 2019), i.e., multiple attractors can coexist in the brain's dynamical landscape. Such multistability begs the question of whether examining the overall layout of the brain's attractor states could better inform or complement what we know about the structure-function relation than explorations around a single state.

Intrinsic brain dynamics have long been observed (Berger, 1929; Bishop, 1932) but often treated as a baseline subtracted from task-positive activities. This baseline, however, is more active than meets the eye: it consumes the largest fraction of the brain's energy resources, while task-related consumption adds little (Raichle and Mintun, 2006). It constrains task performance and related neural activities across multiple time scales (Fox et al., 2006; Ligeois et al., 2019; Schroeder and Lakatos, 2009), and contributes to alteration in neurological and psychiatric disorders (Ayub et al., 2021; Bluhm et al., 2009; Garrity et al., 2007; Green et al., 2017; Zhang and Raichle, 2010). In contrast to the restless dynamics is the (relatively) static structure—the anatomical connections between brain regions, which can be estimated non-invasively using large-scale tractography from diffusion-weighted images (Basser et al., 2000). How can one compare the ever-changing with the unchanging? From a statistical perspective, one may compute the time-averaged features of the dynamics, such as the correlation between signals generated by two brain regions across time—a common measure of functional connectivity. Such functional connectivity patterns can be directly compared to structural ones through linear correlation (Damoiseaux and Greicius, 2009). From a dynamics perspective (Breakspear, 2017; Deco et al., 2011, 2013a), the strength of anatomical connections can be incorporated as constant parameters in a system of differential equations, i.e. a dynamical system. The dynamical

* Correspondence authors.
E-mail addresses: mengsen_zhang@med.unc.edu (M. Zhang), saggar@stanford.edu (M. Saggar).

https://doi.org/10.1016/j.neuroimage.2022.119401.
Received 4 January 2022; Received in revised form 16 May 2022; Accepted 17 June 2022
Available online 19 June 2022.

system, in turn, describes how the state of a model brain, endowed with realistic anatomy, would evolve over time. The time series generated by the model brain and the derived functional connectivity patterns can then be fitted to that of the real brain. Thus, a dynamical system naturally bridges between the unchanging structure and the ever-changing dynamics.

One popular dynamical systems modeling approach is to simulate the noise-driven dynamics near a chosen attractor, such as the low activity ground state, and compare it to the human resting brain dynamics (see Cabral et al. (2017) for a summary of different approaches). Such noise-driven exploration of a single attractor has been shown to exhibit key features of human resting brain dynamics, especially near criticality (e.g. Deco et al. (2013b); Demirta et al. (2019); Ghosh et al. (2008)). On the other hand, noise-driven exploration beyond a single attractor—across multiple attractors or "ghost" attractors—has been shown to capture non-stationary resting brain dynamics and the switching between different dynamic functional connectivity patterns (Deco et al., 2009; Deco and Jirsa, 2012; Golos et al., 2015; Hansen et al., 2015). The best fit to empirical data is often found near the onset of multistability (Deco and Jirsa, 2012; Golos et al., 2015). These observations suggest that examining the layout of the attractor repertoire over the entire multistable landscape could be crucial for understanding the organization of resting brain dynamics (c.f. Golos et al. (2015)).

Complementing existing single-attractor approaches, the present work focuses on the deterministic features of the multistable landscape and examines their empirical relevance. Specifically, we systematically study the organization of the attractor repertoire as a window into the overall shape of the dynamic landscape. We focus on two complementary features of the attractor repertoire: (1) to what extent the states of any two brain regions are correlated across all attractors, which we refer to as cross-attractor coordination, and (2) the distribution of energy gaps between the attractors, which indicates how difficult it is to move across attractors. Mathematically, the former describes in which directions the attractors fall in line with each other in the state space, and the latter describes the spacing between attractors in a predefined direction (such a direction can represent the whole brain or a specific subnetwork). Empirically, we examine how cross-attractor coordination relates to empirically observed functional connectivity between brain regions, and how energy gaps impose a cost on the realization of specific functional connectivity patterns. For constructing the landscape, we use a Wilson-Cowan type biophysical network model that formally combines the reduced Wong-Wang model (Deco et al., 2014, 2013b; Wong and Wang, 2006) and the Wilson-Cowan model (Wilson and Cowan, 1972, 1973). We first showed that the model exhibits extensive multistability, i.e. a large repertoire of attractors to serve as landmarks of the landscape. Further, the model also allows us to examine, computationally and analytically, how structural features across scales shape this repertoire. It is important to note that here we used a broader definition of structural features and not only include large-scale structural connectivity between brain regions, but also local recurrent connectivity within regions, and biophysical constraints at the cellular level. Using this modeling framework and a small dataset from the Human Connectome Project (HCP; n=100; Van Essen et al, 2013), we provide evidence with regards to how the cross-attractor relations in the repertoire could better capture key features of human resting functional connectivity and how such features are shaped by structural features across scales. Finally, we provide a novel framework to analyze the energy constraints for such cross-attractor coordination across different local and global structures.

2. Results

2.1. The model

Whole-brain dynamics are modeled as the mean-field activity of neuronal populations in each brain region. We use a Wilson-Cowan type model (Wilson and Cowan, 1972, 1973), which is also an adapted version of the Wong-Wang model (Deco et al., 2014; Wong and Wang, 2006) with a sigmoidal transfer function (equation S11). The adaptation improves the biological plausibility and multistability upon the reduced Wong-Wang model. Here, we briefly introduce the model; an extensive analysis of the numeric and mathematical properties of the model is provided in the Supplementary Materials (Section S4 for numeric results, Section S8-S9 - for analytical results). Each model region contains a pair of excitatory (E) and inhibitory (I) populations, whose activity is described by the *local model* Fig. 1a, left box; equation 1-(3) in terms of the state variables S_E and S_I. Physically, S_E and S_I are interpreted as the fraction of open synaptic channels in their respective populations, i.e. the gating variables. Through local connections (w's), the excitatory population excites itself with strength w_{EE} and the inhibitory population with strength w_{EI}, while the inhibitory population inhibits itself with strength w_{II} and the excitatory population with strength w_{IE}. Local models further connect to each other through a global network Fig. 1a, dashed lines), giving rise to the *global model* (right; equation 4-(6). For the global model, nodes of the large-scale network correspond to anatomical regions in the human brain based on a 66-region parcellation used in Deco et al. (2013b) and Hagmann et al. (2008) (Fig. 1b). Edge weights of the network reflect the strength of long-range structural connectivity between the brain regions (C_{ij} in equation 6), either estimated using structural data from the Human Connectome Project (Civier et al., 2019; Van Essen et al., 2013) (Section 4.5.1) or artificially constructed for comparison. The overall strength of long-range connections in the model brain is scaled by a global coupling parameter G (equation 6), which denotes the overall level of inter-regional interaction across the whole-brain. In similar modeling approaches, G is typically treated as a free parameter to be fitted to the empirical fMRI data (e.g., Deco and Jirsa (2012); Deco et al. (2014, 2013b); Demirta et al. (2019)). It was thought to be an indicator of the level of arousal or wakefulness (Jobst et al., 2017). In the present work, we first examine theoretically how parameter G influences the dynamic landscape of the model (Fig. 4) and then fit it to individual subjects' fMRI data.

In the present work, the local and global models are used in two ways: (1) to compute the repertoire of attractors using zero-finding algorithms (see Section 4.2 for details) and (2) to be numerically integrated to generate simulated brain dynamics. The former is used to characterize the overall organization of the model dynamic landscape. The latter is used to characterize local explorations of the dynamic landscape. Both aspects are compared to the human data to demonstrate the empirically relevant features. Below, we first illustrate the concept of a dynamic landscape and cross-attractor coordination using a toy example, which is followed by more realistic models to examine how structural properties across scales affect the dynamic landscape.

2.2. Multistable landscape of the brain shaped by structural properties across scales

We begin this subsection with a brief introduction to basic dynamical systems concepts necessary for understanding the results. Readers who are highly familiar with dynamical systems concepts such as attractors, phase transitions, and bifurcations should feel free to skip the following paragraph together with Figs. 2 and 3.

We first introduce basic dynamical systems concepts using a toy model of a single brain region (Fig. 2), and then show how inter-regional synchronization arises within this conceptual framework using a toy model of two-region coordination (Fig. 3). The dynamics of a single brain region is here governed by a potential landscape (black curves in Fig. 2a-c for three different landscapes). When the brain state is in the bottom of a valley (red balls), it is stable and referred to as an attractor. When the brain state is on a peak, it is unstable and referred to as an repeller (black ball). These landscapes can continuously deform into one another under the variation of a control parameter (Fig. 2d),

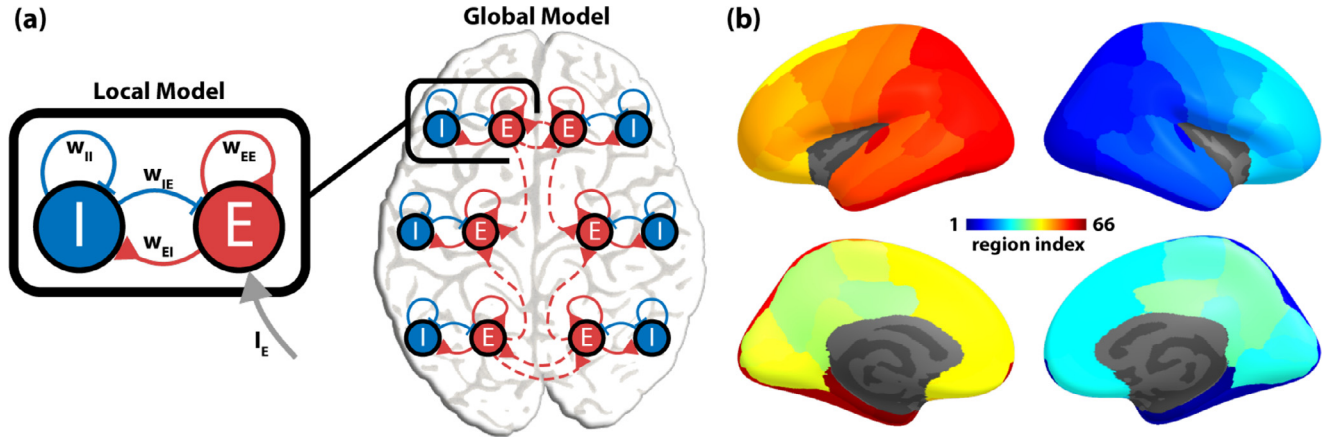

Fig. 1. A dynamic mean-field model of the human brain. (a) The model brain (global model) consists of a network of brain regions (local model). The local model (black box) describes the interaction between two local neural populations — one excitatory (E) and one inhibitory (I). The two populations are coupled via two excitatory connections (red; w_{EE} and w_{EI}) and two inhibitory connections (blue; w_{II} and w_{IE}). The excitatory population of each brain region can further receive input (gray arrow, I_E) from other regions via long-range structural connections (red dashed curves). (b) Nodes in the global model correspond to 66 anatomical regions of the human brain, which can be linked together by the human connectome (see text). Regions are indexed from 1 to 66 (1-33 on the right hemisphere, 34-66 on the left hemisphere in reverse order, following Deco et al. (2013b)). Specific region names are listed in Table S1.

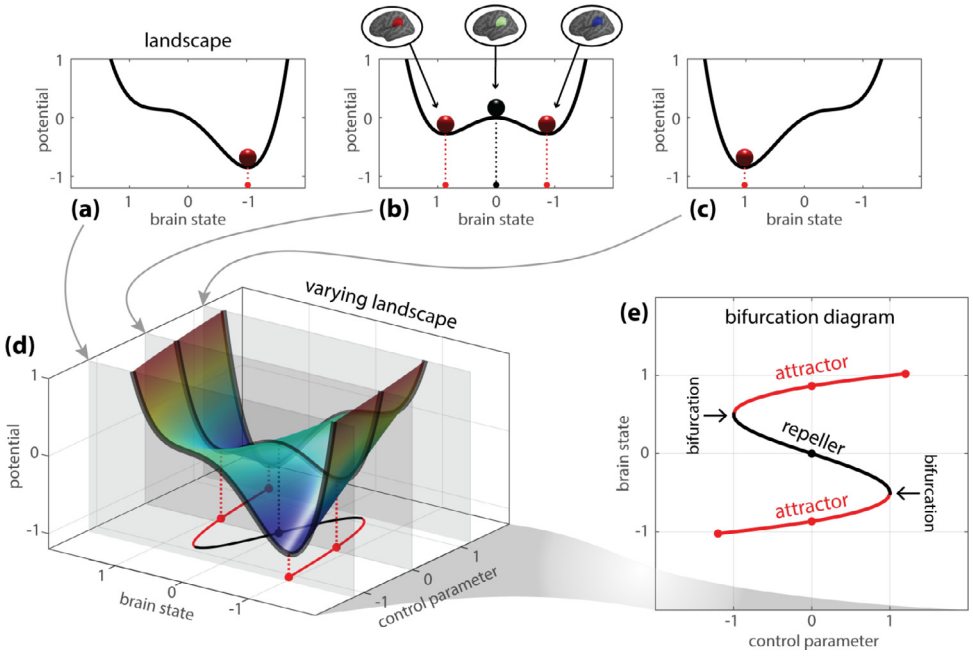

Fig. 2. Conceptual illustration of single-region dynamic landscapes and a bifurcation diagram. (a-c) Dynamics of a single brain region is here governed by a landscape, where the valleys represent the stable states, or attractors, and the peaks represent unstable states, or repellers. (d) The dynamic landscape of the region can be deformed or controlled by an external parameter (control parameter) such as the current input from other regions. The variation of the dynamic landscape with respect to the control parameter can be studied through the variation of its attractors and repellers, shown as points projected to the bottom plane. This simplified representation, which depicts how the attractors and repellers depend on the continuous changes of the control parameter, is called a bifurcation diagram (e). In the bifurcation diagram, each attractor traces out a stripe (two red lines) under the continuous change of the control parameter. At critical values of the control parameter (± 1), one attractor is annihilated by the repeller and disappears. This process is referred to as a bifurcation.

for example, the total level of current input from other brain regions. A bifurcation diagram (Fig. 2d bottom plane, Fig. 2e) keeps track of how the landscape changes with the control parameter via the location of attractors and repellers. At certain points, an attractor disappears by merging into a repeller, which is called a bifurcation. Now, let us consider a slightly augmented toy model that involves two interacting brain regions, i.e., the left and right hemisphere (Fig. 3). An attractor in this toy model represents a stable pattern of activation over the whole brain, shown as boxed brains in Fig. 3. The dynamic landscape determines a repertoire of attractors, different combinations of regional states, with possible paths of transitions between them. Fig. 3a shows such a toy landscape with four attractors (i-iv), each with a different whole-brain activation map. Similar to the single-region landscape, the 3D landscape can be deformed by changes in a control parameter (such as different levels of inter-regional coupling, not shown), which may lead to the creation or destruction of specific attractors through bifurcations (e.g., Fig. 3, a to c, a to b). Such creation and destruction of attractors cause a discrete change of the attractor repertoire, and the set of possible transitions. Note that here a transition refers to a change in *state*, where as a bifurcation refers to a change in the *attractor repertoire*. A bifurcation can trigger a transition if the system was in a state/attractor that is destabilized during the bifurcation; given sufficient noise, a spontaneous transition can occur without a bifurcation. Further, changes in the attractor repertoire can alter how the brain regions coordinate with each other. Two example bifurcations are shown in Fig. 3b-c. In Fig. 3b, only two out of four attractors are left, such that the brain can now only transition between attractor (i) and (iii), thereby leading both hemispheres to be in sync (on or off together). This coordination of brain regions (or hemispheres) can be captured by estimating the cross-attractor coordination matrix (shown in Fig. 3). Similarly, in Fig. 3c, three out of four attractors are left after bifurcation, leading to more complex coordination between brain regions (or hemispheres). Fig. 3d-f presents a more complex example, where a finer parcellation is used and each brain region can now take three activation values (instead of just on

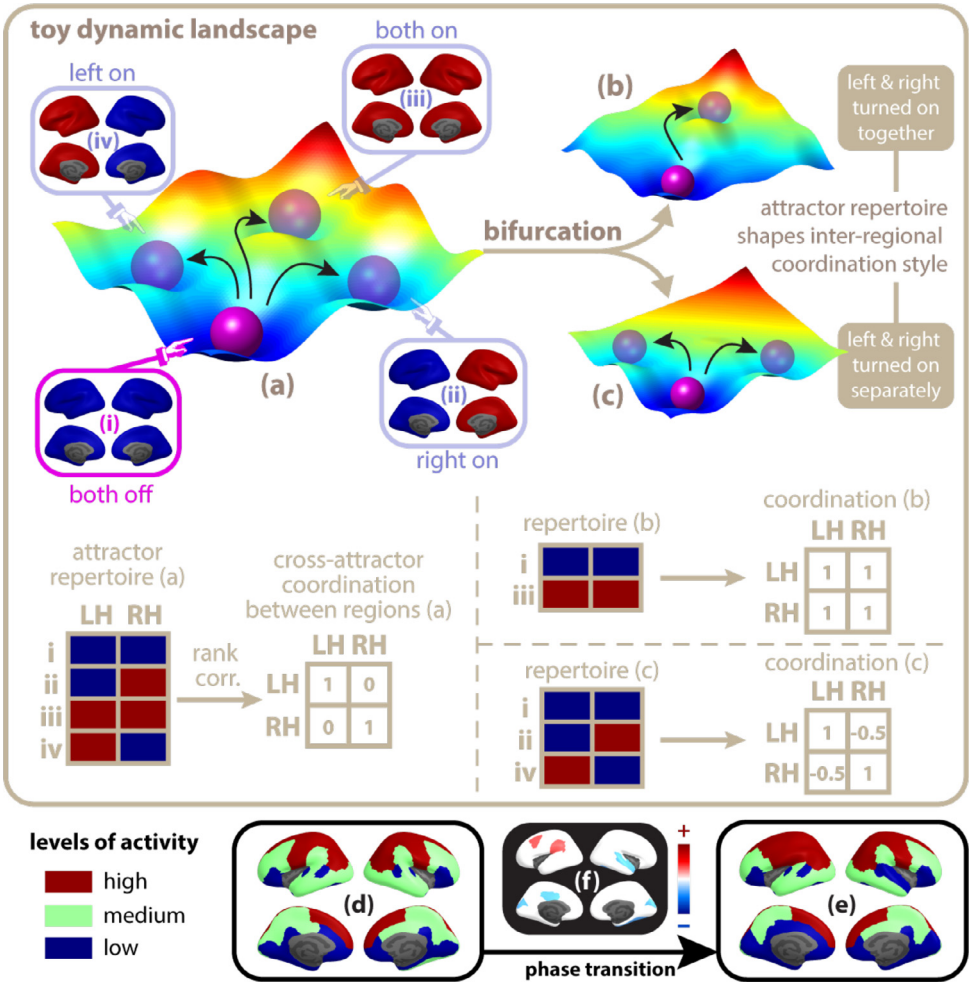

Fig. 3. Conceptual illustration of the whole-brain dynamic landscape, bifurcation, and phase transition. A multistable dynamic landscape (a) contains multiple attractors, shown as troughs occupied by purple balls. Each attractor corresponds to a distinct pattern of activation over the whole brain (i-iv). Influenced by external input or intrinsic noise, the model brain may transition from its current state (attractor i, bright purple ball) to a different one (ii, iii, or iv, dim purple balls), indicated by black arrows. Structural features of a model brain can alter the shape of the landscape, causing some attractors to appear or disappear through a process mathematically named a bifurcation (a→b, a→c, or the reverse). By modifying the repertoire of attractors, bifurcation alters the set of possible transitions and the coordination between regions during transitions. For example, in landscape (a), the left and right hemisphere can be co-activated during a transition (i→iii), or activated separately through other transitions (i→ii, or i→iv). In contrast, in landscape (b), the left and right hemisphere can only be co-activated, and in (c), only activated separately. Numerically, a repertoire of attractors can be represented as a matrix, where each row represents an attractor and each column represents a brain region (repertoire matrix a, b, c, with entries shown as blue/red color blocks). The overall inter-regional coordination across attractors can be estimated by the rank correlation between the columns of the repertoire matrix. The resulted square coordination matrix summarizes how brain regions transition together over the entire landscape, serving as a signature of the landscape (coordination matrix a, b, c, shown to the right of each repertoire). In more complex landscapes (not shown), there are many more attractors, and they correspond to subtler patterns of activation (d,e; see also Fig. 4). The coordination between brain regions during a transition is correspondingly more complex (f=e-d), with some regions co-activated (red) while others co-deactivated (blue).

or off), resulting in more complex spatial activation patterns across the whole brain as well as complex coordination between brain regions. See Section 4.3 for technical details about how the coordination matrix is estimated.

Next, we present a set of more realistic examples to show how local as well as global structural connectivity of the brain can shape the dynamic landscape, its associated repertoire of attractors and their transitions. Here, we depict dynamic landscapes and their changes as bifurcation diagrams (Fig. 4; see Section 4.2 for computational details). Fig. 4 shows nine different bifurcation diagrams, across its three rows and columns. The rows correspond to bifurcation diagrams from: (first row: a-c) a single brain region (local model); (second row: d-f) the entire brain with uniform connectivity across all brain regions; and (third row: g-i) the entire brain with realistic connectivity across all brain regions. Thus, the second and third rows of Fig. 4 aim to depict the effect of changes in global structural connectivity on the dynamical landscape. The columns, on the other hand, in Fig. 4 aim to depict the effect of changes in local connectivity, i.e., level of excitation within the individual brain regions, on the dynamic landscape.

In each bifurcation diagram, the y-coordinate of each *colored* point indicates the position of an attractor: here we use the average activity of all excitatory populations $\bar{S}_E$ (Fig. 4d-i; black points are repellers). The x-coordinate indicates the value of a control parameter, which modulates the shape of the underlying dynamic landscape: here we use the overall strength of long-range connections—the global coupling G (equation 6). Further, each vertical slice of a bifurcation diagram contains the repertoire of attractors and repellers in a fixed landscape (an example slice is shown in Fig. 4h), corresponding to stable and unstable patterns of brain activity respectively. Lastly, an attractor traces out a horizontal "stripe" as it changes continuously with the landscape (examples shown in Fig. 4d-i). A colored stripe merges with a black stripe at a bifurcation, where an attractor is annihilated by a repeller. The number of colored stripes indicates the complexity of the landscapes, i.e., more stripes indicate more attractors.

Locally within each model brain region, the dynamics are controlled by local structural connectivity (w's in Fig. 1a; see Section S4 for detailed numeric results and Section S8 for analytical results). In particular, a single model region can switch between a rich set of dynamic regimes by varying the excitatory-to-excitatory connections (w_{EE}) and the excitatory-to-inhibitory connections (w_{EI}; Figure S1). Fig. 4a-c show the bifurcation diagrams for three local connectivity settings from three distinct dynamic regimes (regime e, d, and a respectively in Figure S1). With an overall increase of local excitatory connectivity from (a) to (c), a single region becomes more complex—more attractors and stronger oscillatory activities.

To understand the effects of global connectivity, we first examined the brain dynamical landscape where all regions are uniformly connected with each other Fig. 4d-f). Here, stronger local excitatory connections (e,f) produce a more complex landscape (3 attractor stripes) than weak ones (d; 2 attractor stripes; see Figure for even weaker local connections). These bifurcation diagrams are very similar to those of a single brain region (Fig. 4a-c), in terms of the number of attractors and

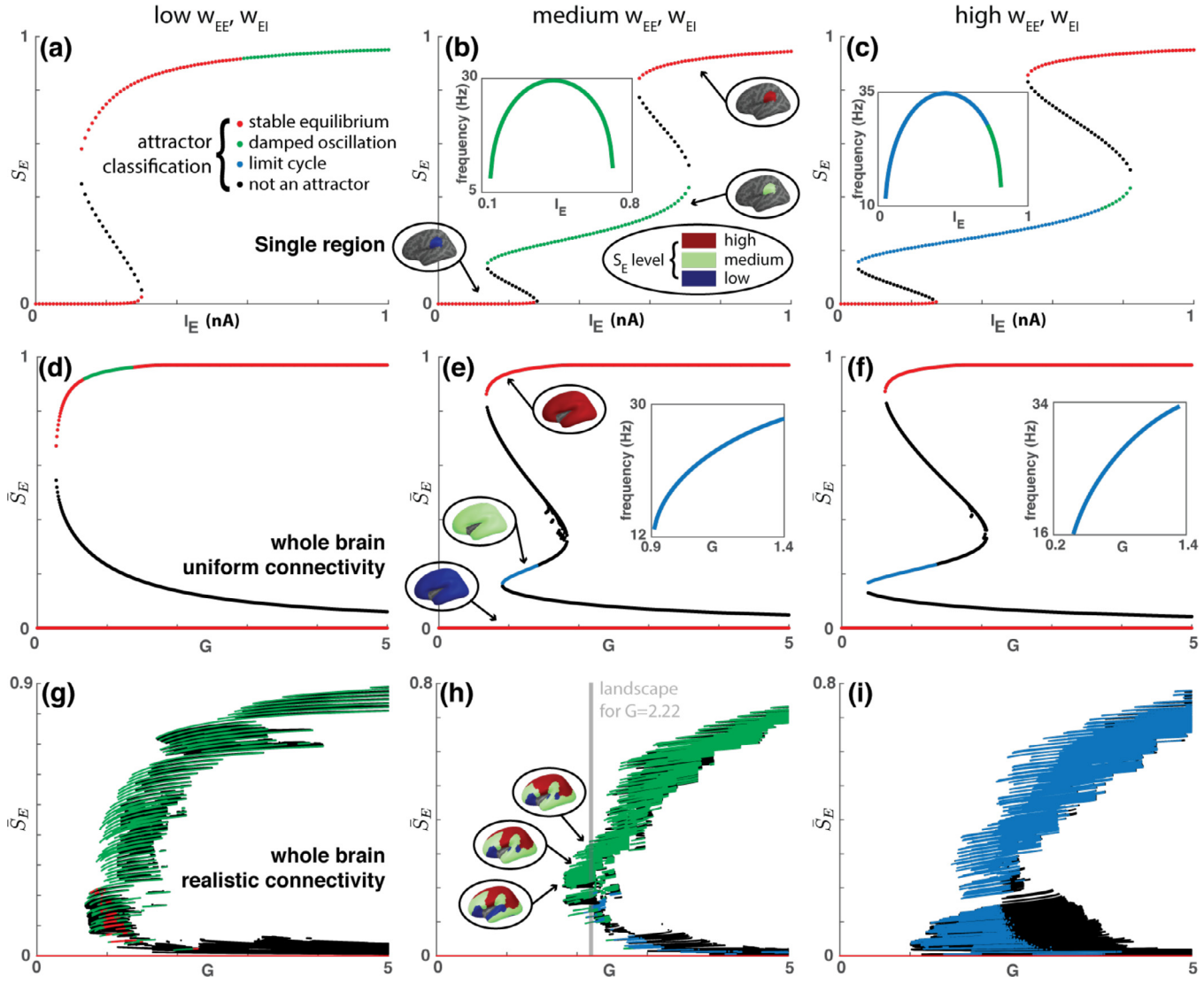

Fig. 4. Local and global structural properties jointly determine the complexity of whole-brain dynamics. (a-c) show the bifurcation diagrams of the local model for three different types of local excitatory connectivity: (a) $w_{EE} = 0.7$ and $w_{EI} = 0.35$; (b) $w_{EE} = 2$ and $w_{EI} = 1$; (c) $w_{EE} = 2.8$ and $w_{EI} = 1$ (representatives of distinct dynamic regimes of the local model, Figure S1). Overall, local connectivity increases from (a) to (c). The activity of the excitatory population S_E is used as an order parameter, indicating the location of each attractor. The external input I_E is used as a control parameter. Each point in the diagram indicates the location of a particular fixed point. The color denotes the type of each fixed point: non-black points represent attractors, black points unstable fixed points that are not associated with a limit cycle. Horizontal stripes indicate that the attractors are changing continuously with the control parameter for a certain range. All (a)-(c) have an upper stripe and a lower stripe. (b)-(c) have an additional stripe in the middle, where the brain region oscillates. Insets of (b) and (c) show the oscillation frequency of the brain region as a function of the input current. Each stripe corresponds to a discrete level of activation for a single brain region (circled brains in b; color indicates discrete S_E levels, shown in circled legend). (d)-(f) show the corresponding bifurcation diagrams for three uniform global networks, i.e. the large-scale structural connectivity C_{ij}'s are identical between any two brain regions (equation 6). The average activity of all excitatory populations ($\bar{S}_E$) is used as an order parameter and the global coupling G (equation 6) as a control parameter. Each attractor stripe corresponds to a pattern of activation over the whole brain (circled brains in (e) show $S_E^{(i)}$'s on the left hemisphere). Similarly, (g)-(i) show the corresponding bifurcation diagrams for three realistic global networks, i.e. C_{ij}'s reflect the human connectome (see text for details). Here each vertical slice (gray line in h) contains the attractor repertoire of a fixed dynamic landscape shaped by the human connectome. Each attractor repertoire is associated with a matrix describing the coordination between brain regions across attractors (e.g. Fig. 5b). See Fig. 3 for a cartoon illustration of attractor repertoires and the associated cross-attractor coordination matrices.

the presence of oscillation. In fact, the whole brain (Fig. 4e) moves up and down together between discrete states of activation, very much like a single region (Fig. 4b). Note that, for the global model (equation 4-(6) to be multistable, a minimal amount of global coupling is required, i.e., $G > 1$ (Fig. 4d-f). If the brain regions act independently ($G = 0$), both the individual regions (Fig. 4a-c at $I_E = 0$) and the whole brain (Fig. 4d-f at $G = 0$) are monostable—there is only one stable pattern of activity, where the gating variables are all close to zero. This result indicates that a functionally complex brain can emerge out of the synergistic interaction between simple regions. Additional analytical and numerical results are provided in Section S9 (Multistability) for further validation and generalization.

Next, we show that in addition to the global coupling G, the details of inter-regional connections matter too (C_{ij} in equation 6). Given a realistic global structural connectivity (human connectome; Fig. 4g-i), the complexity of the whole-brain dynamic landscape increases dramatically: 171 attractor stripes in (g), 610 in (h), and 682 in (i) (per single-linkage clustering). Correspondingly, the patterns of activation (Fig. 4h) are more complex, with greater differentiation between regions; the coordination between brain regions across attractors is consequently more

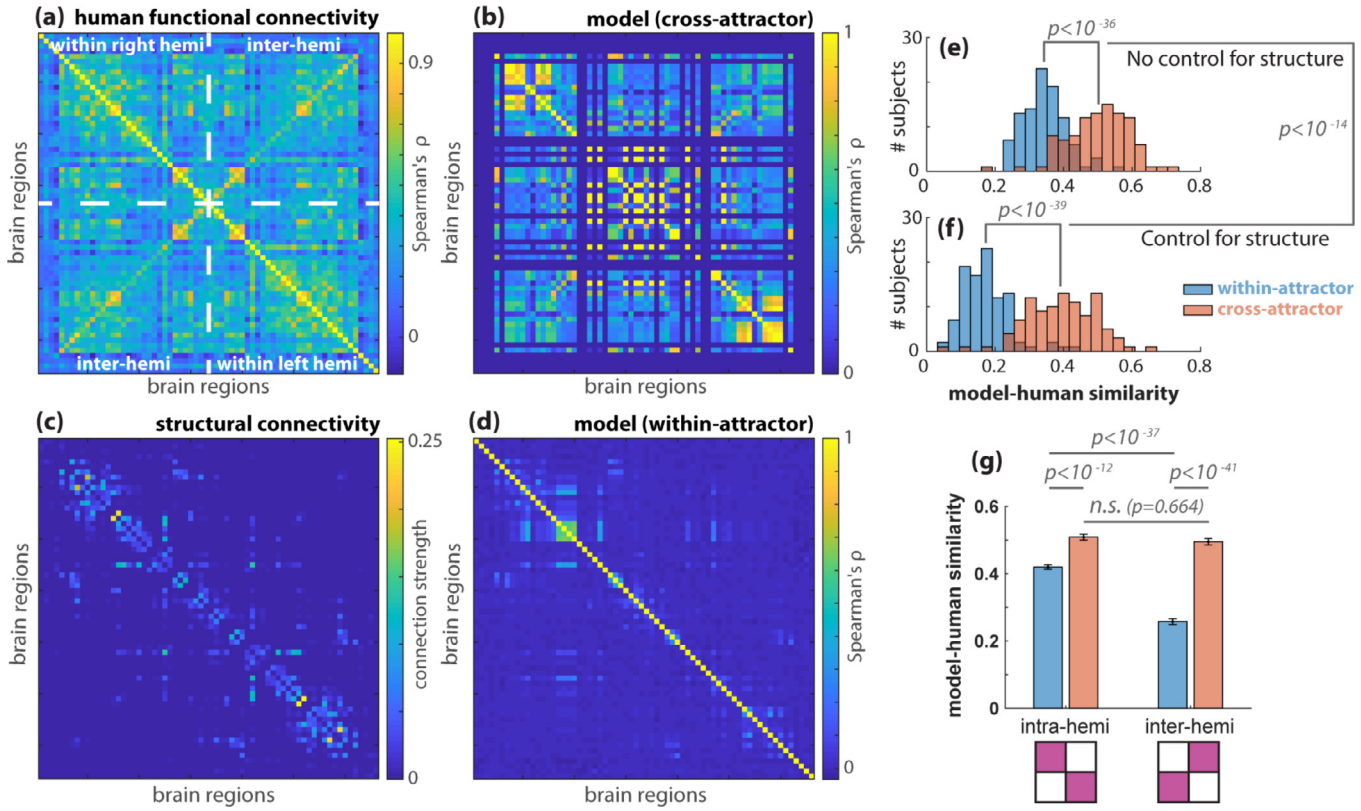

Fig. 5. Cross-attractor coordination captures large-scale symmetry of human functional connectivity and its nonlinear dependency on structure better than within-attractor coordination. An example of human functional connectivity matrix (a) is calculated using the resting fMRI data from the Human Connectome Project (Van Essen et al., 2013), averaged over 11 unrelated subjects. The average structural connectivity of the same subjects is shown in (c). Regions (columns and rows) are ordered symmetrically for the left and right hemispheres (see Fig. 1b) to reveal the large-scale symmetry of resting brain dynamics (ordering follows Deco et al. (2013b); see the complete list of region names in Table S1). White dashed lines delineate the matrix (a) into four blocks, describing the functional connectivity within the right hemisphere (upper left block), within the left hemisphere (lower right), and between two hemispheres (lower left/upper right). Functional connectivity patterns within the hemispheres are similar to each other and similar to inter-hemispheric connectivity patterns. The symmetry between intra- and inter-hemispheric connectivity is well captured by inter-regional coordination in the model brain across attractors (b) ($w_{EE} = 2$, $w_{EI} = 1$, $G = 2.22$ for local maximum model-human similarity; c.f. Fig. 4h gray slice). Such symmetry is not captured by the coordination within any of the said attractors (d; best fit within-attractor coordination matrix). When examined across individuals (using n=100 unrelated HCP participants), a significantly better model-human similarity was obtained when cross-attractor coordination was used instead of within-attractor coordination (e); the difference between cross-attractor coordination and within-attractor coordination with respect to model-human similarity is even greater when partial correlation is used to control for the contribution of structural connectivity (f). Comparing intra-hemisphere and inter-hemisphere functional connectivity separately (g), we found that cross-attractor coordination captures human intra- and inter-hemisphere functional connectivity equally well (red bars), while within-attractor coordination is better at capturing intra-hemisphere than inter-hemisphere functional connectivity (blue bars). The distributions of correlation coefficients were obtained through a model fitting procedure with the same local parameters ($w_{EE} = 2$, $w_{EI} = 1$) while allowing the G parameter to vary from 1.7 to 3.0 by steps of 0.1.

flexible and subtle (as depicted in Fig. 3f). The heterogeneous nature of the human connectome breaks the large-scale spatial symmetry of the model brain, creating more functional differentiation between brain regions and greater functional complexity for the whole brain. In short, the complexity of the global dynamical landscape is a joint product of strong local excitatory connection and complex topology of the large-scale network. See Section S9 for additional analytical supports.

2.3. *Cross-attractor coordination reveals large-scale symmetry of human brain functional connectivity*

In this section, using data from the Human Connectome Project (HCP) (Van Essen et al., 2013), we present both qualitative and quantitative results to show how cross-attractor coordination could better capture key features of human resting functional connectivity than noise-driven within-attractor coordination. For qualitative results, we used averaged structural and functional connectivity across subjects from a smaller HCP cohort (n=11 individuals), whereas for the quantitative results, we used individual structural and functional connectivity estimates across all 100 unrelated individuals from the HCP data.

Typically, human functional connectivity (FC) is calculated from the fMRI data by estimating co-fluctuations across brain regions. The estimated resting state FC matrix usually reflects large-scale symmetry across the two hemispheres, such that brain regions across the two hemispheres highly co-fluctuate (i.e., high antidiagonal values in Fig. 5a). For qualitative results, we used averaged structural and functional connectivity matrices across a small subset of the HCP n=11 unrelated individuals (see Section 4.5 for more details). Using averaged structural connectivity matrix, a dynamical landscape Fig. 4h) was generated and cross-attractor coordination was estimated for a chosen $G = 2.2$. At the selected G, 97 attractors were found. Mathematically, each attractor is represented by a row vector denoting the activity level of all brain regions (equation 8-(9). Thus, for a chosen G, using the (#attractors × #regions) matrix we estimated the cross-attractor coordination between regions (equation 10), such that regions that co-fluctuate across attractors tend to show high cross-attractor coordination (or similarity). See Section 4.2 for mathematical details and Fig. 3a-c for an intuition regard-

ing the estimation of cross-attractor coordination matrix. As shown in Fig. 5b, the dominant feature of human resting state FC, i.e., large-scale symmetry across brain regions, is well preserved in the cross-attractor coordination matrix. Such inter-hemispheric symmetry is not seen in stochastic within-attractor coordination (Fig. 5d). Moreover, the pattern of within-attractor coordination is a closer reflection of the human structural connectivity (Fig. 5c) than the human functional connectivity (Fig. 5a).

Next, to examine the model fit on an individual basis, we ran a quantitative analysis using the n=100 unrelated-individuals cohort of the HCP data (Van Essen et al., 2013). Our results confirm that cross-attractor coordination can better predict human functional connectivity than within-attractor coordination. The maximum model-human correlation for cross-attractor coordination has an average Spearman's Rho of 0.50 (S.D. 0.09), while the correlation for within-attractor coordination has an average of 0.34 (S.D. 0.06) (Fig. 5d). That is, on average, cross-attractor coordination explains 25.0% of the variance in human FC, while within-attractor coordination explains 11.6% of the variance in human FC. Based on within-subject paired t-test, cross-attractor coordination provided significantly better fit of FC ($t(99) = 20.2$, $p < 10^{-36}$; Fig. 5e). To understand how the two types of models relate to the underlying structural connectivity, we calculate the partial correlation between model coordination matrices and human functional connectivity, controlling for the linear contribution of structural connectivity. With the contribution of structural connectivity controlled, the model-human correlation for cross-attractor coordination has an average Spearman's Rho of 0.39 (S.D. 0.10), which is significantly greater than that of the within-attractor coordination 0.17 (S.D. 0.07) (Fig. 5f; $t(99) = 21.9$, $p < 10^{-39}$). That is, excluding the contribution of structural connectivity, cross-attractor coordination explains 15.2% of the variance in human FC, while within-attractor coordination explains 2.9% of the variance in human FC. 40% of the explanatory power of cross-attractor coordination comes from structural connectivity, while 75% of the explanatory power of within-attractor coordination comes from structural connectivity. Furthermore, the difference between the partial correlation coefficients for the cross-attractor coordination and the within-attractor coordination (0.22 ± 0.10) is significantly greater than that of the regular correlation coefficients (0.16 ± 0.08) with $t(99) = 9.5$ and $p < 10^{-14}$ (Fig. 5f vs. Fig. 5e), which suggests that within-attractor coordination is more linearly dependent on the structural connectivity. Finally, we show that the model-human similarity for inter-hemisphere coordination is significantly lower than that of intra-hemisphere coordination for within-attractor coordination but not for cross-attractor coordination (Fig. 5g). In other words, unlike within-attractor coordination, cross-attractor coordination captures human intra- and inter-hemisphere functional connectivity equally well.

To understand how variability in individual model parameters translates into measures of behavior, individual parameters were correlated with a measure of fluid intelligence, an abbreviated version of the Raven's Progressive Matrix Test (PMAT). Correlating the model parameters with measures of fluid intelligence showed one significant result. Specifically, the strength of the model-human similarity and the number of correct responses on the test was significantly correlated (Spearman's Rho = 0.21, p = 0.04) after controlling for age and sex. All other correlations with fluid intelligence measures were not significant.

2.4. Structural connectivity defines the energy demands of cross-attractor coordination

In the above section, we computed the cross-attractor coordination matrices (equation 10 in Section 4.3), which only concerns whether two brain regions move up and down together across the dynamic landscape, but not how difficult or metabolically expensive such movements are. In this section, we examine the "energy gaps" between the attractors, and how they are shaped by local and structural properties of the model. Fig. 6a gives a conceptual illustration of the relation between attractors and the energy gaps between them. Each attractor is associated with an average level of activity or energy ($\bar{S}_E$; equation 11) given a fixed parameter G. There is an energy gap between each pair of adjacent attractors (equation 12; see a full technical description in Section 4.3). In the subject-average model (n=11, HCP; Fig. 4g-i), the average and maximum energy gap clearly vary with local connectivity (w_{EE}, w_{EI}) and global connectivity (G), here summarized in Fig. 6b. Quantitatively, stronger local connections reduce the energy gaps (Fig. 6c,d), and stronger global connections (G) increase the energy gaps (Fig. 6b)—local and global structural connectivity pull the energy cost in different directions.

Next, we examine the effect of energy constraints on model fit. Without energy constraints, the computation of the cross-attractor coordination assumes that the brain could traverse arbitrarily large energy gaps, while in reality, crossing very large energy gaps may be unrealistic. To incorporate the effect of energy constraints (see Section 4.3 for detailed methods), we split an ordered attractor repertoire into sub-repertoires between which the energy gap is considered too high. Thus, we obtain a sub-repertoire above the maximum energy gap, equation 13, and a sub-repertoire below the maximum energy gap, equation 14. Cross-attractor coordination matrices computed within the sub-repertoires can be considered as energy-constrained coordination patterns between brain regions. Fig. 7a-c shows that such energy-constrained cross-attractor coordination (dashed lines) is more sensitive to different structural features in its ability to capture human functional connectivity. The energy constraint inflicts a greater loss of model-human similarity when the local structural connectivity is weak (area of the shaded region shrinks from Fig. 7a to c, and bars in d decreases with increasing local connectivity from left to right) and the global structural connectivity is strong (height of shaded regions grows with G in Fig. 7a-c). The loss of similarity grows with the maximum gap size (Fig. 7d; $\rho = 0.96$, $p<10^{-100}$ for $w_{EE} = 0.7$ and $w_{EI} = 0.35$; $\rho = 0.92$, $p<10^{-100}$ for $w_{EE} = 2$ and $w_{EI} = 1$; $\rho = 0.85$, $p<10^{-100}$ for $w_{EE} = 2.8$ and $w_{EI} = 1$). This indicates that models fitted with a high value of G may implicate an unrealistic level of high-energy-cost transitions. When cross-attractor coordination matrices were fitted to n=100 unrelated HCP subjects (Fig. 5e), the optimal G is 2.5 ± 0.28 (Fig. 7e). The corresponding maximum energy gaps average to 0.12 ± 0.08 (Fig. 7f), and the corresponding mean energy gaps average to 0.009 ± 0.015 (Fig. 7f). Thus, the optimal cross-attractor models in the present study are located in a realistic regime, which is least affected by energy constraints (Fig. 7d, max energy gap<0.2).

3. Discussion

The present work examines how the brain's multistable dynamic landscape can be shaped by structural features across scales and what features of the landscape are relevant to empirical observations. Complementing the previous stochastic noise-driven exploration approach, the present work focuses on the deterministic features of the multistable landscape and examines their empirical relevance. We demonstrate that large-scale symmetries of human functional connectivity patterns and their nonlinear dependency on the structure could be better explained by the relation between attractors in the landscape than the property of any individual attractor. Thus, the present work offers a novel cross-attractor perspective on resting brain dynamics, equipped with a computational framework to produce empirical relevant summaries of the attractor repertoire in full as well as in parts.

The functional complexity of the model brain is controlled by both local and global structural connectivity. At the level of a single isolated brain region, the dynamic repertoire can be effectively controlled by two key local structural properties: local excitatory-to-excitatory connectivity (self-excitation) and local excitatory-to-inhibitory connectivity. In the real brain, local excitatory-to-excitatory connections are particularly abundant (Somogyi et al., 1998), and in the model brain, they contribute indispensably to multistability (Section S8). Multistability is a key source of biological complexity from molecular to social lev-

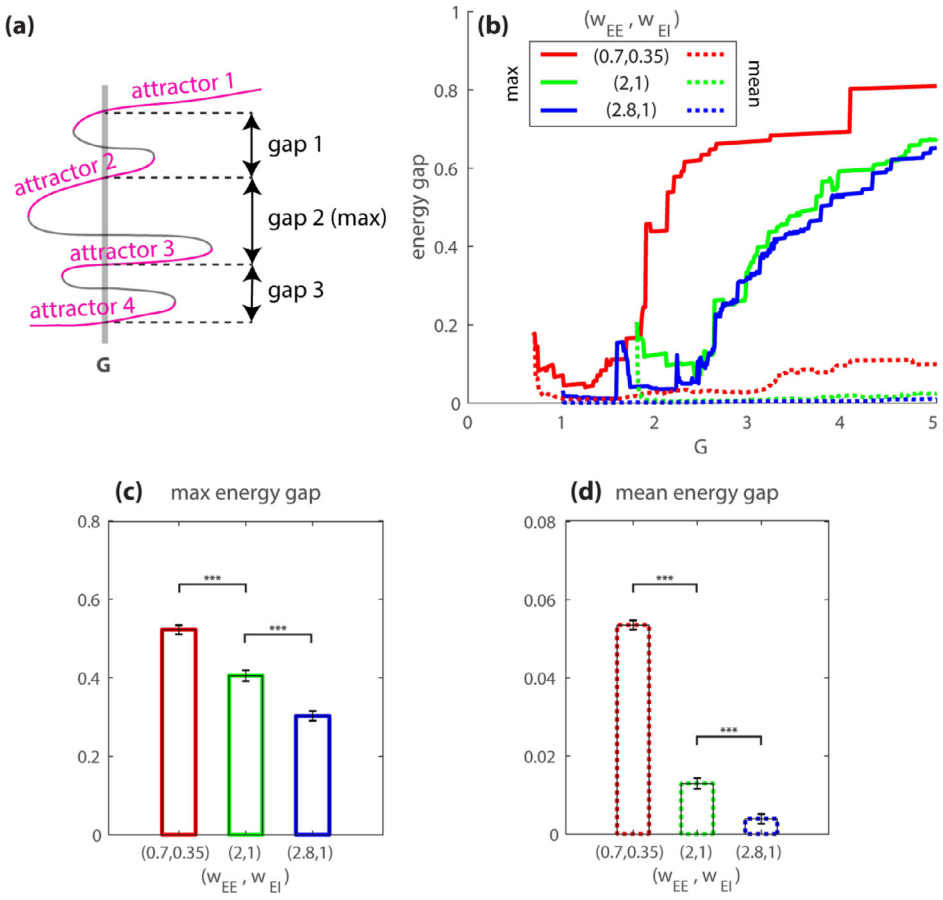

Fig. 6. Local (w_{EE}, w_{EI}) and global (G) structural connectivity jointly shape the energy cost of cross-attractor coordination. (a) gives a conceptual illustration of the relation between attractors and energy gaps with a toy bifurcation diagram. The average and maximum gap sizes are of our interest. (b-d) summarize the size of energy gaps between attractors shown in Fig. 4g-i (subject-average model with n=11). (b) Overall, the maximum (solid lines) and average energy gaps (dashed lines) increase with global coupling G, though there is a transient decrease when the maximum energy gap is less than 0.2. Both types of gaps decrease with increasing local connectivity w_{EE}, w_{EI} (c,d). (*** p<0.001 with Bonferroni correction. Error bars are standard errors.)

els (Laurent and Kellershohn, 1999; Zhang et al., 2019), often tied to self-excitation or positive feedback (Angeli et al., 2004; Arthur, 1990; Attneave, 1971). Manipulating the model's local excitatory-to-excitatory connections have physical implications. The recurrent excitatory synaptic properties of the present model is determined by the conductance of the N-methyl-D-aspartate (NMDA) receptors (Wong and Wang, 2006). Thus, modulating excitatory-to-excitatory connectivity in the model can be interpreted empirically as modulating the conductance of NMDA receptors in local neuronal populations, using, for example, pharmacological and endogenous antagonists and agonists such as ketamine (Orser et al., 1997) and dopamine (Wang et al., 2012). Such manipulations have been theoretically predicted and shown to affect memory capacity (Anticevic et al., 2012; Murray et al., 2014; Verma and Moghaddam, 1996). Note that the strength of local excitatory-to-excitatory connections needs to surpass a critical value to induce the transition from a monostable to a multistable regime (equation S30). In the present work, this critical value is a constant (equation S29), which depends on cellular-level properties such as the membrane time constant and the gain of the input-output response. Thus, manipulating such microscopic properties can induce, or remove, multistability from a single brain region.

At the large-scale network level, multistability can be created or amplified by the synergistic interaction between mono- or multi-stable brain regions. Different large-scale network structures have dramatically different capabilities at amplifying local complexity: a realistic global network is much more powerful than a uniform one. The human connectome breaks the spatial symmetry of the global model, whereas symmetry breaking is often a key to complex dynamics (Golubitsky and Stewart, 2002; Golubitsky et al., 1999; Kelso, 1995; Kelso et al., 2013; Pillai and Jirsa, 2017; Tognoli and Kelso, 2014). On the other hand, the human connectome is endowed with more specific features such as modularity, small-worldness, and multiscale characteristics (Sporns, 2002, 2004, 2011; Sporns and Tononi, 2001). A systematic study of how these features alter the geometry of the global dynamic landscape is worthy of further theoretical investigation (see Section S9).

Within the multistable landscape sculpted by the human connectome, inter-regional coordination across attractors exhibits key features of human functional connectivity patterns. Such cross-attractor coordination better captures human functional connectivity than within-attractor coordination—synchronization between brain regions within the same basin of attraction. This finding raises the possibility that functional connectivity patterns reflect transitions between stable brain states more than the brain states themselves.

A transition-based, or cross-attractor, view on functional connectivity has several theoretical and empirical implications. First, it provides an explanation for the large-scale symmetry of human FC, i.e., the similarity between intra- and inter-hemispheric connectivity patterns. It has been noted that within-attractor dynamics of similar models lack such symmetry, exhibiting weak inter-hemispheric FC (Deco et al., 2013b; Demirta et al., 2019). The weak inter-hemispheric FC has been attributed to an underestimation of structural connections across hemispheres using diffusion-weighted imaging. This explanation is reasonable given that within-attractor dynamics can be approximated by a linear dynamical system, which closely depends on the structural connectivity (Deco et al., 2014, 2013b). Nevertheless, an alternative explanation could be that human FC implicates far-from-equilibrium dynamics where the nonlinearity cannot be ignored (Hansen et al., 2015). It is a signature of nonlinear systems that a small input does not necessarily produce a small effect. Indeed, strong functional connectivity in humans is known to exist between regions that are not directly connected (Honey et al., 2009). As we have shown, cross-attractor coordination takes into account such nonlinear effects. Mathematically, our cross-

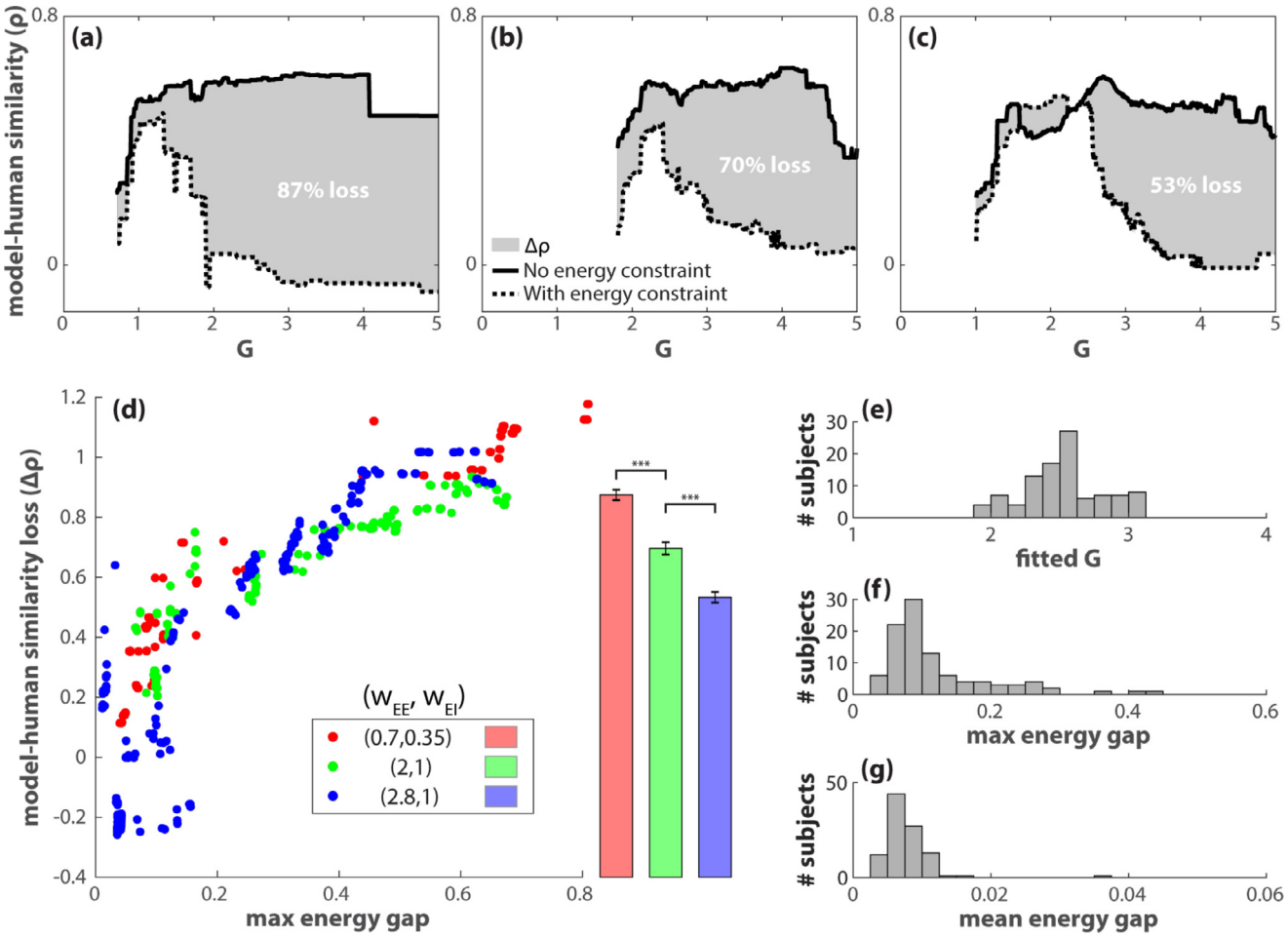

Fig. 7. The loss of model-human similarity due to energy constraints depends on local and global structural features. (a-c) The model-human similarity for cross-attractor coordination (no energy constraint, black solid lines) is stable with respect to varying global coupling G and local excitatory connectivity w_{EE} and w_{EI} (a: $w_{EE} = 0.7$ and $w_{EI} = 0.35$, b: $w_{EE} = 2$ and $w_{EI} = 1$, c: $w_{EE} = 2.8$ and $w_{EI} = 1$). Dashed lines indicate the model-human similarity when the model is energy-constrained, i.e., it does not cross the maximum energy gap between attractors. This 'energy-constrained' similarity is computed by splitting the attractor repertoire into two sub-repertoires, one above the maximum energy gap and one below it (c.f. Fig. 6a). The cross-attractor coordination within each sub-repertoire is compared to the human functional connectivity through Spearman's correlation. The dashed lines indicate the greater correlation coefficient (ρ) among the two subrepertoires. The shaded area ($\Delta\rho$) indicates the loss of model-human similarity due to the energy constraint. (d) Each point in the scatter plot represents the percent loss of model-human similarity for not crossing the maximum energy gap, given a specific combination of global coupling G and local connectivity w_{EE} and w_{EI}. Overall, the loss increases with the maximum gap size, which in turn depends on G (Fig. 6b). The average loss (bars in d) decreases with increasing local excitatory connectivity (w_{EE}, w_{EI}). When the cross-attractor model was fitted to individual subjects (using n=100 unrelated HCP participants; c.f. Fig. 5e), the optimal global connectivity G (e) and the corresponding maximum energy gap (f) and mean energy gap (g) are low, where the cross-attractor coordination is least affected by energy constraints. (*** $p<0.001$ with Bonferroni correction. Error bars are standard errors.)

attractor approach amounts to studying the relation between the zeros of a nonlinear function—a problem that does not admit a linear approximation. The symmetry between intra- and inter-hemispheric connectivity is likely to reflect a symmetry of the set of all zeros, i.e. the (roughly) invariance of the zero set under the exchange of variable indices between the homologous regions of the left and right hemispheres. The invariance of the zero set is, in turn, consequent to the invariance of the differential equations under such a left-right reflection. A full mathematical treatment of the problem is beyond the scope of the present study. Nevertheless, it invites theoretical investigations of the symmetry groups of nonlinear neural dynamical models (c.f. Golubitsky and Stewart, 2002).

The second implication is that the cross-attractor view is compatible with treating functional connectivity as both stationary and dynamical. Cross-attractor coordination, when measured over the entire dynamic landscape, is itself time-invariant. Empirically observed stability and convergence of human functional connectivity (Gordon et al., 2017; Laumann et al., 2016) may reflect this invariance of the underlying landscape. The static landscape can also support dynamic functional connectivity (dFC) (Hansen et al., 2015; Hutchison et al., 2013). At any given time, the possible transitions depend on the attractor currently dwelled upon. Thus, in a short time window, cross-attractor coordination is confined to a subset of attractors. In this perspective, dFC reflects the transitions between attractors in a subset of the repertoire. As a consequence, a state-based and a dFC-based representation of neural dynamics may diverge—subsets of attractors that are close in the state space may have distinct patterns of transitions, and subsets of attractors that are far apart in the state space may have similar patterns of transitions. In other words, precaution may be used when treating dFC patterns as brain states.

Finally, the cross-attractor view attaches the concept of energy costs to functional connectivity patterns. In this perspective, the potential for exhibiting, say, normal resting-state functional connectivity patterns may always be there, but the energy costs modulate the difficulty for such potential to be realized. It is especially interesting to consider the potential "costs" of functional connectivity patterns in relation to cogni-

tive functions and psychiatric disorders. The energy gaps in the present framework can be calculated within a subnetwork relevant to a specific cognitive function. An individualized fitting of the model for a subnetwork may help predict how difficult it is for a subject to perform a specific type of tasks. Further, examining the energy gap distributions in people with psychiatric disorders may help elucidate the network mechanisms underlying the pathology. The neural and behavioral correlates of the energy gaps could be further explored. It is reasonable to assume that a greater energy gap between two attractors is associated with a lower probability of transition and thus a lower probability of observing the corresponding cross-attractor coordination. The cross-attractor coordination over pairs of, rather than the whole repertoire of, attractors maps may be compared to dynamic functional connectivity in empirical analysis. Extending the present framework to the study of dynamic functional connectivity is a worthy future direction. The use of simultaneous PET-fMRI may provide more direct evidence for metabolic measures. To further examine how the energy gaps may affect cognition, causal manipulations such as non-invasive brain stimulation (e.g., transcranial magnetic stimulation) or pharmacological interventions (e.g., Methylphenidate) are required.

Like all scientific studies, the present work has several limitations. First, although cross-attractor coordination better fits human data than within-attractor coordination, a large portion of the variance in the human FC remains unaccounted for. Incorporating additional individualized model parameters may further improve the model fit: for example, an estimate of the local recurrent connectivity for each brain region and long-range inhibitory connectivity between brain regions. Nevertheless, there may be a fundamental limit to what biologically realistic parameters may be estimated from non-invasive measures of the human brain. Second, the present study has not explored whether increasing the dimensionality of the model will lead to a better model fit. Two obvious ways to increase the dimensionality of the model is to increase the number of local excitatory and inhibitory populations included in each model brain region (Golos et al., 2015), and/or to use a finer parcellation of the whole brain (Demirta et al., 2019). Both approaches would likely increase the number of attractors and repellers of the model, providing a more refined estimate of cross-attractor coordination. In the present study, the choice of parcellation and the two-population local model was primarily based on the convention adopted by existing modeling studies using the predecessors of our present model (Deco et al., 2014; Demirta et al., 2019; Ponce-Alvarez et al., 2015). Identifying a precise scaling law of the number of attractors as a function of the number of parcels and the number of local populations is beyond the scope of the present study but is worthy of further investigation. Future research should also address what minimal complexity/dimensionality of the model is required to achieve a near-optimal fit. Third, the present work only focuses on resting-state fMRI data in a neural typical population. To understand brain functional connectivity in a broader context, the computational framework can be extended to study the changes in functional connectivity driven by external stimulation or due to psychiatric disorders. Future experimental validation of the present framework could utilize fMRI recorded from subjects under non-invasive brain stimulation such as transcranial direct current stimulation (tDCS), transcranial alternating current stimulation (tACS), or transcranial magnetic stimulation (TMS). For a most direct example, tDCS generates a static electric field over the brain, creating different levels of current flow in different brain regions. Simulated regional currents can be incorporated into the model as constants I_E and I_I in equation 1-2. As non-invasive brain stimulation is increasingly used as a treatment for psychiatric disorders such as major depressive disorder (Alexander et al., 2019; Avery et al., 2006; Brunoni et al., 2016), a modeling framework based on dynamical systems principles may play an important role in the future improvement of treatment designs (Zhang et al., 2022). Fourth, the present study did not fully explore how features of the model dynamic landscape can help predict behavioral traits or performances of the subjects. One may expect the model to yield better predictions for tasks or behavior that involve interhemispheric coordination. Examples of such tasks include bimanual motor coordination (Gerloff and Andres, 2002; Schöner and Kelso, 1988) and language processing involving the non-dominant (right) hemisphere (Doron et al., 2012). Future research may explore the correlation between, for example, energy gaps for interhemispheric coordination between relevant brain regions with subjects' motor and language skills.

In summary, the present work examines intrinsic brain dynamics in terms of an underlying landscape and the repertoire of stable activity patterns it affords. Model-based analyses reveal that empirically observed functional connectivity patterns may reflect transitions between activity patterns more than the patterns themselves. The work outlines a modeling framework that emphasizes the *relation* between stable activity patterns. It is thus suitable for examining systemic changes in the brain that result in interrelated improvement or impairment in multiple cognitive and affective functions, such as in development and psychiatric disorders.

4. Materials and Methods

4.1. The present model

The local model is described by the equations,

$$\frac{\mathrm{d}\,S_E}{\mathrm{d}\,t} = -\frac{S_E}{\tau_E} + (1 - S_E)\gamma_E\, H_E(w_{EE}S_E - w_{IE}S_I + I_E) \tag{1}$$

$$\frac{\mathrm{d}\,S_I}{\mathrm{d}\,t} = -\frac{S_I}{\tau_I} + (1 - S_I)\gamma_I\, H_I(w_{EI}S_E - w_{II}S_I + I_I). \tag{2}$$

S_E and S_I are the gating variables of the excitatory and inhibitory population respectively (Fig. 1a), which indicate the fraction of open channels in each population. The activity of each population has a natural decay time of τ_E or τ_I, which are the time constants of the NMDA and GABA receptors (Table S2) respectively. The model is a mean-field reduction of a network of leaky-integrate-and-fire neurons, where the slow integration time of the NMDA receptors dominates over the fast dynamics of the AMPA receptors (Wong and Wang, 2006) (see also Section S3). Each population's activity tends to increase with the fraction of closed channels $(1 - S_p)$ and the population firing rate (H_p), scaled by a factor γ_p for $p \in \{E, I\}$. This is described by the second term on the right-hand-side of equation 1-2. H_E and H_I are transfer functions that map synaptic current input to population firing rate of the excitatory and the inhibitory population respectively. In particular, they are sigmoidal functions of the form

$$H_p(x) = \frac{r_{max} + \dfrac{a_p x - b_p - r_{max}}{1 - e^{d_p(a_p x - b_p - r_{max})}}}{1 - e^{-d_p(a_p x - b_p)}}, \tag{3}$$

whose output increases with input monotonically and saturates at r_{max}—the maximum firing rate limited by the absolute refractory period of neurons (around 2 ms in certain cell types; see Andersen et al. (1978), Yeomans (1979)). The specific shape of each transfer function is determined by three additional parameters a_p, b_p and d_p (a_p and b_p determine the location and slope of the near-linear segment in the middle; d_p determines the smoothness of the corners bordering the said near-linear segment). This transfer function is converted from Wong and Wang's original formulation (Abbott and Chance, 2005; Wong and Wang, 2006) (a soft rectifier function, equation S6) into a sigmoidal form, while retaining the original value of parameters a_p, b_p, and d_p (shown in Table 1). As a result, the present model is a Wilson-Cowan type model (Wilson and Cowan, 1972, 1973). The parameters were chosen to approximate the average response of a population of spiking pyramidal cells ($p = E$) and interneurons ($p = I$) respectively, incorporating physiologically plausible parameters (Wang, 2002; Wong and Wang, 2006).

Interaction between local populations is modulated by four coupling parameters $w_{pq} \geqslant 0$ in equation 1-2, indicating the influence from the local population p to q, where $p, q \in \{E, I\}$ (Fig. 1 left box). These coupling

Table 1
The interpretation and value of model parameters. Here we summarize the parameters used in equation 1-5. Most parameters assume a fixed value, which was introduced by Wong and Wang (2006). A "~" indicates that this parameter is manipulated in the present study to explore the behavior of the model or to fit the model to empirical data. For local connectivity, three pairs of values were used in the present study for w_{EE} and w_{EI}, which are (0.7, 0.35), (2, 1), and (2.8, 1). These parameters were chosen from three different regimes of the local model (regime e, d, a in Figure S1-S2), which are dominated by stable fixed points, damped oscillations, and sustained oscillations respectively. w_{IE} matches w_{EE} to provide feedback inhibition (Deco et al., 2014). These values fall within a range comparable to that of existing studies (Deco et al., 2014; Demirta et al., 2019). The constant excitatory input I_E to the local model ranges between 0 and 1 to demonstrate how the dynamics of a single brain region can be altered by inputs from other regions (Fig. 4). When modeling resting brain dynamics using the global model I_E is zero, assuming no external input to the brain. G ranges between 0 and 5, used to explore the effect of global coupling on multistability (Fig. 4) and to fit the model to empirical data. The range of G used was consistent with that of existing studies (Deco et al., 2014; Demirta et al., 2019). C_{ij} is defined by each subject's structural connectome. The noise amplitude σ is set to zero for verifying the classification of fixed points, is set to 0.01 when calculating within-attractor coordination, following Deco et al. (2014).

parameter	interpretation	value
τ_E	decay time of NMDA receptor	0.1 (s)
τ_I	decay time of GABA receptor	0.01 (s)
γ_E	kinetic parameter of excitatory population	0.641
γ_I	kinetic parameter of inhibitory population	1
a_E	parameter of H_E	310 (nC^{-1})
b_E	parameter of H_E	125 (Hz)
d_E	parameter of H_E	0.16 (s)
a_I	parameter of H_I	615 (nC^{-1})
b_I	parameter of H_I	177 (Hz)
d_I	parameter of H_I	0.087 (s)
r_{max}	maximum firing rate	500 (Hz)
w_{EE}	excitatory-to-excitatory coupling	~ (nA)
w_{EI}	excitatory-to-inhibitory coupling	~ (nA)
w_{IE}	inhibitory-to-excitatory coupling	~ (nA)
w_{II}	inhibitory-to-inhibitory coupling	0.05 (nA)
I_E	external input to excitatory population	~ (nA)
I_I	external input to inhibitory population	0.1 (nA)
G	global coupling	~ (nA)
C_{ij}	structural connectivity between brain regions	~
σ	noise amplitude	~

parameters reflect the local structural connectivity. The local populations are also capable of responding to external current inputs denoted as I_E and I_I in equation 1-2, respectively. Importantly, such input can come from other brain regions in a globally connected network (Fig. 1 right panel, dashed lines). This leads us to the global model. Formally, we substitute I_E in the local model (equation 1) with a global input I_G (equation 4),

$$\frac{\mathrm{d}S_E^{(i)}}{\mathrm{d}t} = -\frac{S_E^{(i)}}{\tau_E} + (1 - S_E^{(i)})\gamma_E H_E\left(w_{EE}^{(i)} S_E^{(i)} - w_{IE}^{(i)} S_I^{(i)} + I_G^{(i)}(\vec{S}_E)\right) + \sigma\xi_E^{(i)}(t) \tag{4}$$

$$\frac{\mathrm{d}S_I^{(i)}}{\mathrm{d}t} = -\frac{S_I^{(i)}}{\tau_I} + (1 - S_I^{(i)})\gamma_I H_I\left(w_{EI}^{(i)} S_E^{(i)} - w_{II}^{(i)} S_I^{(i)} + I_I\right) + \sigma\xi_I^{(i)}(t) \tag{5}$$

where $S_E^{(i)}$ and $S_I^{(i)}$ are the synaptic gating variable of the excitatory and the inhibitory population of the i^{th} brain region respectively, and $\xi_\cdot^{(i)}$ is a noise term scaled to an amplitude σ. The state of all excitatory populations is denoted as a vector $\vec{S}_E$, the i^{th} element of which is $S_E^{(i)}$. The global input to the i^{th} brain region depends on both its connectivity with, and the ongoing state of, other brain regions,

$$I_G^{(i)}(\vec{S}_E) = G\sum_{\substack{j=1\\ j\neq i}}^{N} C_{ij} S_E^{(j)} \tag{6}$$

where N denotes the total number of brain areas, $C_{ij} \geqslant 0$ the long-range structural connectivity from the j^{th} to the i^{th} brain region and G is a global coupling parameter that controls the overall level of interaction across brain regions. Since C_{ij} is only intended to represent long-range connectivity, we let $C_{ij} = 0$ for any $i = j$ to preclude recurrent connections. For the effects of G and C_{ij} to be independently comparable, here we impose a normalization condition on the matrix norm,

$$\|\mathbf{C}\|_\infty = \max_i\left(\sum_{j=1}^{N}|C_{ij}|\right) \equiv 1. \tag{7}$$

Since the global coupling parameter G modulates the level of input to each brain region, one would expect it to have comparable influence on the local dynamics as I_E in the local model (equation 1).

4.2. Computation of attractors and bifurcation diagrams

The repertoire of attractors and bifurcation diagrams Fig. 4) are computed in MATLAB, utilizing the build-in function `fsolve`. Given a proper initial guess, `fsolve` finds the coordinates of a nearby fixed point of the dynamical system (e.g., the local model, equation 1-2, or global model, equation 4-(5) and calculates the corresponding Jacobian matrix. Given N model brain regions, the spectrum $\{\lambda_k\}_{k=1}^{2N}$ of the Jacobian matrix is used to classify the fixed points and identify which ones are attractors. The fixed point is a stable equilibrium if λ_k is real and negative for all k. The fixed point is associated with damped oscillation if $\mathrm{Re}\,\lambda_k < 0$ for all k and $\mathrm{Im}\,\lambda_k \neq 0$ for some k. The fixed point is associated with a limit cycle if $\mathrm{Re}\,\lambda_k > 0$ and $\mathrm{Im}\,\lambda_k \neq 0$ for some k with the additional criteria that after a small perturbation from the fixed point, the time-average of the solution remains close to the fixed point. The above three types of fixed points—a stable equilibrium, a stable spiral (damped oscillation), a fixed point associated with a limit cycle (sustained oscillation)—represent attractors in the present study. All other types of fixed points are classified as unstable. For damped oscillation and limit cycles in the local model, the frequency of the oscillation (Figure S1) is defined as $|\mathrm{Im}\,\lambda_k|/(2\pi)$.

For the local model, a 2D dynamical system, the complete characterization of all fixed points is relatively easy by searching exhaustively through a grid of initial guesses (as for Fig. 4a-c). This approach becomes unfeasible when it comes to the global model due to the high dimensionality. Thus, for the global model (Fig. 4d-i), we implemented a recursive search: for each value of G, (1) find zeros of equation 4-6 using `fsolve` given a set of initial guesses that includes, if any, the zeros for $G - \delta G$ ($\delta G = 0.01$ for the present study) in addition to a fixed set of grid points; (2) sort the list of zeros obtained from (1) by the average of $S_E^{(i)}$'s denoted as $\bar{S}_E$; (3) use the middle points between consecutive zeros in the sorted list as initial guesses; (4) continue to use middle points between past initial guesses as new initial guesses recursively until at least one new zero is found or the recursion has reached a certain depth; (5) append the new zero(s) to the list of zeros and repeat (2)-(5) until the number of identified zeros exceeds a certain value. In the present study, we limit the maximum depth in (4) to 8 and the maximum number of zeros in (5) to 200. The set of zeros so obtained are the fixed points of the dynamical system. Each fixed point is further classified using the respective Jacobian matrix as described above to identify the attractors—a subset of the fixed points forming the attractor repertoire.

For each set of structural parameters (G, $\mathbf{C}$, w_{EE}, w_{EI}), we represent the attractor repertoire as a M-by-N matrix,

$$\mathbf{A}(G, \mathbf{C}, w_{EE}, w_{EI}) = \begin{bmatrix} S_{E,1}^{(1)} & S_{E,1}^{(2)} & \cdots & S_{E,1}^{(N)} \\ S_{E,2}^{(1)} & S_{E,2}^{(2)} & \cdots & S_{E,2}^{(N)} \\ \vdots & \vdots & \ddots & \vdots \\ S_{E,M}^{(1)} & S_{E,M}^{(2)} & \cdots & S_{E,M}^{(N)} \end{bmatrix} \tag{8}$$

where M is the number of attractors, and N is the number of brain regions.

As parameters vary (e.g., G in Fig. 4d-i), the attractors form discrete connected components (e.g., stripes in Fig. 4) in the product of the state space and the parameter space. Attractors within the same connected

component can be considered qualitatively equivalent, as they morph into each other under continuous parameter change. Understanding the relation between these connected components are critical to characterizing phase transitions and bifurcations. It is thus meaningful to define a discretized version of the attractor repertoire,

$$\hat{\mathbf{A}}(G,\mathbf{C},w_{EE},w_{EI})=\begin{bmatrix}\hat{S}_{E,1}^{(1)} & \hat{S}_{E,1}^{(2)} & \cdots & \hat{S}_{E,1}^{(N)}\\ \hat{S}_{E,2}^{(1)} & \hat{S}_{E,2}^{(2)} & \cdots & \hat{S}_{E,2}^{(N)}\\ \vdots & \vdots & \ddots & \vdots\\ \hat{S}_{E,M}^{(1)} & \hat{S}_{E,M}^{(2)} & \cdots & \hat{S}_{E,M}^{(N)}\end{bmatrix} \tag{9}$$

where $\hat{S}_{E,i}^{(j)}$ is positive integer representing a discrete level of activation which $S_{E,i}^{(j)}$ belongs to (see Fig. 3 for toy examples). Each row vector in equation 9 gives the multi-index of an attractor connected component. In practice, the mapping between the continuous level $S_{E,i}^{(j)}$ to the discrete levels of $\hat{S}_{E,i}^{(j)}$ can be created by partitioning the continuous interval [0,1] at the minima of the distribution of all $S_{E,i}^{(j)}$'s (see Section S7 for examples). Examining the properties of $\mathbf{A}$ and $\hat{\mathbf{A}}$ opens the door to systematic characterization of the underlying dynamic landscape.

4.3. Quantifying cross-attractor coordination and energy gaps based on the attractor repertoire

Given a discretized attractor repertoire $\hat{\mathbf{A}}$ (equation 9), the cross-attractor coordination matrix is an N-by-N matrix,

$$\mathbf{P}(G,\mathbf{C},w_{EE},w_{EI})=\begin{bmatrix}\rho(\hat{A}_{\cdot,1},\hat{A}_{\cdot,1}) & \rho(\hat{A}_{\cdot,1},\hat{A}_{\cdot,2}) & \cdots & \rho(\hat{A}_{\cdot,1},\hat{A}_{\cdot,N})\\ \rho(\hat{A}_{\cdot,2},\hat{A}_{\cdot,1}) & \rho(\hat{A}_{\cdot,2},\hat{A}_{\cdot,2}) & \cdots & \rho(\hat{A}_{\cdot,2},\hat{A}_{\cdot,N})\\ \vdots & \vdots & \ddots & \vdots\\ \rho(\hat{A}_{\cdot,N},\hat{A}_{\cdot,1}) & \rho(\hat{A}_{\cdot,N},\hat{A}_{\cdot,2}) & \cdots & \rho(\hat{A}_{\cdot,N},\hat{A}_{\cdot,N})\end{bmatrix} \tag{10}$$

where $\hat{A}_{\cdot,j}$ denotes the j^{th} column of $\hat{\mathbf{A}}$ and $\rho(x,y)$ the Spearman's correlation between variables x and y (see Fig. 3 for toy examples, Fig. 5b for a more elaborate example). Spearman's correlation is chosen to reflect the ordinal nature of the variable $\hat{S}_{E,i}^{(j)}$. $P_{i,j}=\rho(\hat{A}_{\cdot,i},\hat{A}_{\cdot,j})$ gives the level of cross-attractor coordination between model brain region i and j. The use of the *discretized* attractor repertoire $\hat{\mathbf{A}}$ ensures that coordination matrix $\mathbf{P}$ is invariant within the same dynamic regime and only changes during a bifurcation. Thus, matrix $\mathbf{P}$ connects the change of brain coordination patterns to dynamical systems concepts such as bifurcation—a qualitative change in the dynamic landscape of the model brain.

The coordination matrix $\mathbf{P}$ by itself does not explicitly concern how difficult or energy consuming these cross-attractor movements are. To incorporate energetic properties, we equip each attractor repertoire with a sequence of energy gaps. We first order the rows of the attractor repertoire matrix $\mathbf{A}$ so that the row averages descend with the row index. The row averages of the ordered repertoire matrix provide a sequence of energy levels,

$$\mathbf{e}(G,\mathbf{C},w_{EE},w_{EI})=\begin{bmatrix}\bar{S}_{E,1}\\ \bar{S}_{E,2}\\ \vdots\\ \bar{S}_{E,i}\\ \vdots\\ \bar{S}_{E,M}\end{bmatrix} \tag{11}$$

where $\bar{S}_{E,i}=N^{-1}\sum_{j=1}^{N}A_{ij}$, $\bar{S}_{E,i}>\bar{S}_{E,i+1}$ for any $i<M$, and M is the number of attractors. The corresponding energy gaps are

$$\Delta\mathbf{e}(G,\mathbf{C},w_{EE},w_{EI})=\begin{bmatrix}\bar{S}_{E,1}-\bar{S}_{E,2}\\ \bar{S}_{E,2}-\bar{S}_{E,3}\\ \vdots\\ \bar{S}_{E,i-1}-\bar{S}_{E,i}\\ \vdots\\ \bar{S}_{E,M-1}-\bar{S}_{E,M}\end{bmatrix}, \tag{12}$$

where $\Delta e_i=\bar{S}_{E,i-1}-\bar{S}_{E,i}$ is the energy gap between the $(i-1)^{\text{th}}$ and i^{th} attractor in the repertoire. Physically, each energy gap Δe_i can be interpreted as the energy cost associated with keeping additional x% synaptic channels open. Synaptic transmission is a major energy consumer in the brain (Harris et al., 2012). For example, the opening of NMDA receptors are associated with presynaptic, postsynatpic, and astrocytic costs, estimated to be roughtly 70k ATPs per vesicle released and 10^8 ATPs per action potential generated (Attwell and Laughlin, 2001). The sequence of energy gaps can be used to partition the attractor repertoire into sub-matrices. For example, if Δe_i is the maximum energy gap, one can split $\mathbf{A}$ (and its discretized version $\hat{\mathbf{A}}$) into a repertoire above the energy gap

$$\mathbf{A}_{+}(G,\mathbf{C},w_{EE},w_{EI})=\begin{bmatrix}A_{1,\cdot}\\ A_{2,\cdot}\\ \vdots\\ A_{i-1,\cdot}\end{bmatrix}, \tag{13}$$

and a repertoire below the energy gap

$$\mathbf{A}_{-}(G,\mathbf{C},w_{EE},w_{EI})=\begin{bmatrix}A_{i,\cdot}\\ A_{i+1,\cdot}\\ \vdots\\ A_{M,\cdot}\end{bmatrix}, \tag{14}$$

where $A_{i,\cdot}$ is the i^{th} row of the ordered repertoire matrix $\mathbf{A}$. Each of the sub-repertoires $\mathbf{A}_{+}$ and $\mathbf{A}_{-}$ is associated with its own cross-attractor coordination matrix, say, $\mathbf{P}_{+}$ and $\mathbf{P}_{-}$ (equation 10). $\mathbf{P}_{+}$ and $\mathbf{P}_{-}$ can be considered as the "energy-constrained" coordination patterns where the model brain is not allowed to cross the energy gap Δe_i. The same line of analysis is applicable to a sub-network of the model brain (e.g., the default mode network) by constructing a reduced repertoire matrix that only contains a subset of the columns in $\mathbf{A}$. These selected columns map to the brain regions within the sub-network. This series of analysis applied to attractor repertoire matrices and sub-matrices provides a systematic and simple way to characterize brain dynamic landscape and inter-regional coordination.

4.4. Estimating within-attractor coordination through simulations

Within-attractor coordination is estimated using conventional methods of numeric simulation. In the present work, for each attractor in the repertoire, the dynamical system equation 4-(6) is integrated using stochastic Heun's method, with a time step of 1 ms, a moderate level of noise $\sigma=0.01$ and a duration $T=864$ s (14 min 33 s to match the human data (Van Essen et al., 2013)). The exact coordinates of the attractor are used as the initial conditions such that the simulated dynamics reflects the noise-driven exploration near that attractor. Conventional correlation analysis is then applied to the simulated time series of the excitatory populations ($S_E^{(i)}$'s) to obtain the functional connectivity matrix (e.g., Fig. 5c). Spearman's correlation is used in accordance with the computation of cross-attractor coordination matrix ($\mathbf{P}$, equation 10).

4.5. Data and methods of analysis

4.5.1. Human structural data

The human structural connectome used in the present study is from the S1200 Release from the Human Connectome Project (HCP) (Van Essen et al., 2013). The average connectome of 11 unrelated subjects were used for the first qualitative analysis (it has been shown that averaging over 5 subjects is sufficient; (see Deco et al. 2013b; Hansen et al. 2015), while the individual connectome of 100 subjects obtained from a previous study (Civier et al., 2019) were used for the second quantitative analysis. For both analyses, the subject-level connectome data are based on the Desikan-Killiany parcellation (Desikan et al., 2006) obtained from Civier et al. (2019), retaining the 66 ROIs used in Hagmann et al. (2008) and Deco et al. (2013b) (Fig. 1b). The original diffusion imaging (dMRI) data were obtained using a customized Siemens

3T scanner at Washington University in St. Louis, with a standard 32-channel head coil, with TR = 5520 (ms), TE = 89.5 (ms), 1.25 (mm) isotropic voxels, b=1000, 2000, 3000 (s/mm^2). T1 images were obtained using 3D magnetization-prepared rapid gradient echo sequence (MPRAGE) with TR = 2400 (ms), TE = 2.14 (ms), and 0.7 (mm) isotropic voxels. The HCP minimally processed data were further processed using *MRtrix3*, including bias-field correction, multi-shell multi-tissue constrained spherical deconvolution with a maximum spherical harmonic degree 8. 10 million probabilistic streamlines were generated for each subject using the 2nd-order Intergration over Fibre Orientation Distributions algorithm (iFOD2) (Tournier et al., 2010) and anatomically-constrained tractography (ACT) (Smith et al., 2012) (FOD amplitude threshold = 0.06, step size = 0.625 mm). Each streamline was assigned a weight using spherical-deconvolution informed filtering of tractograms (SIFT2) (Smith et al., 2015). Connection strengths between ROIs are summed weights of the associated streamlines. Intra-ROI connections are removed. Subjects' connectivity matrices are normalized according to equation 7 before and after averaging.

4.5.2. Human functional data

Human functional connectivity used in the present study is estimated using the resting-state fMRI (rsfMRI) data of the same subjects from the Human Connectome Project (Van Essen et al., 2013) as aforementioned ones from the structural connectivity. rsfMRI scans were acquired using EPI sequences with TR = 720 (ms), TE = 33.1 (ms), flip angle = 52°, voxel size = 2.0 (mm, isotropic), multiband factor = 8. Four runs of rsfMRI scan were obtained from each subject in 2 separate days (2 runs in each day with opposite phase-encoding direction: RL and LR). Each run last 14 min 33 s (1200 TR).

For the first analysis, unprocessed data were downloaded from the Human Connectome Project database (https://db.humanconnectome.org) and preprocessed using *fMRIPrep* 1.4.0 (Esteban et al., 2018b; Esteban et al., 2018a; RRID:SCR_016216), which is based on *Nipype* 1.2.0 (Gorgolewski et al., 2011; Gorgolewski et al., 2018; RRID:SCR_002502). First, a reference volume and its skull-stripped version were generated using a custom methodology of *fMRIPrep*. A deformation field to correct for susceptibility distortions was estimated based on two echo-planar imaging (EPI) references with opposing phase-encoding directions, using `3dQwarp` (Cox and Hyde, 1997) (AFNI 20160207). Based on the estimated susceptibility distortion, an unwarped BOLD reference was calculated for a more accurate co-registration with the anatomical reference. The BOLD reference was then co-registered to the T1w reference using `bbregister` (FreeSurfer) which implements boundary-based registration (Greve and Fischl, 2009). Co-registration was configured with nine degrees of freedom to account for distortions remaining in the BOLD reference. Head-motion parameters with respect to the BOLD reference (transformation matrices, and six corresponding rotation and translation parameters) are estimated before any spatiotemporal filtering using `mcflirt` (FSL 5.0.9, Jenkinson et al., 2002). The BOLD time-series were resampled to the *fsaverage* surface space. Several confounding time-series were calculated including framewise displacement (FD), DVARS and three region-wise global signals. FD and DVARS were calculated for each functional run, both using their implementations in *Nipype* (following the definitions by Power et al., 2014). The three global signals were extracted within the CSF, the WM, and the whole-brain masks.

Nuance regressions were performed on detrended, preprocessed BOLD time series in the *fsaverage* space (FreeSurfer), following procedures in Power et al. (2014). Regressors include 6 motion parameters, CSF signal, WM signal, and their first derivative and second power. Frames with FD>0.2 mm are censored. Spline-interpolated signals are band-pass filtered between 0.009 and 0.08 Hz, and averaged within ROIs based on the Desikan-Killiany parcellation (Desikan et al., 2006). 66 Regions in Hagmann et al. (2008) are retained and ordered according to Deco et al. (2013b) (Fig. 1b). Functional connectivity between ROIs are estimated using Spearman correlation between z-scored time series for each rsfMRI run of each subject. The connectivity matrices are then averaged across all runs/subjects in Day 1 and in Day 2 separately. The average functional connectivity matrix from Day 1 is used in all comparisons with the model. The average functional connectivity matrix from Day 2 is used to assess the reliability of the estimation.

For the second analysis, an alternative preprocessing pipeline that is standard for individual rsfMRI preprocessing was applied. Specifically, minimally preprocessed rsfMRI volumetric data from the HCP database was downloaded and further denoised through application of a published spatial independent component rejection procedure (Glasser et al., 2013; Griffanti et al., 2017; Smith et al., 2013). The resulting rsfMRI timeseries was then converted to ROI space by averaging voxels part of the Desikan-Killiany atlas in volume space (Klein and Tourville, 2012). Relative to the list in Table S1, there were six missing ROIs, which are the left and right temporal pole, the left and right frontal pole, and the left and right bank of the superior temporal sulcus. Similar to the case with the 11 subjects, there were 4 runs per subject (2 runs with opposite encoding for 2 separate days). To calculate the functional connectivity, ROI time series were z-scored and then correlated with Spearman correlation between each pair of ROIs. The resulting 4 connectivity matrices were averaged to obtain one final connectivity matrix per subject.

4.5.3. Individual subject simulation and model fitting

To find the optimal human-model fitting on an individual basis, simulations were run with one representative set of local parameters ($W_{EE} = 2$, $W_{EI} = 1$), while the global coupling parameter was varied from 1.7 to 3.0 with step sizes of 0.1. This set of parameter configurations were chosen with considerations for the run time while capturing the individual variability for the optimal value of G. Additional details of the simulation, including computation of the within and cross attractor coordination, and energy gaps between attractors, were identical to the analysis of the 11 subject averaged data.

Spearman's correlation was used to quantify the model-human correlation. The optimal G parameter for each individual was determined based on the maximum correlation for the cross-attractor coordination. Within-attractor coordination matrices were determined for individual attractors at that optimal G and used to find the highest model-human correlation for within-attractor coordination. To compare the model fit between within and cross-attractor coordination on an individual level, a paired t-test was applied between the model-human correlation for the two across the 100 individuals.

4.5.4. Correlating with measures of fluid intelligence

An abbreviated 24-items version of the Raven's Progressive Matrix Test Form A was used for evaluating fluid intelligence (Bilker et al., 2012; Duncan et al., 2000) and scored with the number of correct responses (PMAT24_A_CR). Spearman's correlation was calculated between model parameters and PMAT24_A_CR while controlling for age and sex. Model parameters of interest include the maximum correlation value, the associated optimal G parameter, and the maximum energy gap at the optimal G.

Credit authorship contribution statement

Mengsen Zhang: Conceptualization, Methodology, Software, Data curation, Validation, Formal analysis, Investigation, Writing – original draft, Visualization. **Yinming Sun:** Data curation, Writing – review & editing, Validation, Investigation, Visualization. **Manish Saggar:** Conceptualization, Resources, Writing – review & editing, Supervision, Project administration, Funding acquisition.

Acknowledgements

This work is supported by a NIH Director's New Innovator Award to M.S. (MH119735).

Supplementary material

Supplementary material associated with this article can be found, in the online version, at doi:10.1016/j.neuroimage.2022.119401.

References

Abbott, L.F., Chance, F.S., 2005. Drivers and modulators from push-pull and balanced synaptic input. Progress in Brain Research 149, 147–155. doi:10.1016/s0079-6123(05)49011-1.

Alexander, M.L., Alagapan, S., Lugo, C.E., Mellin, J.M., Lustenberger, C., Rubinow, D.R., Frohlich, F., 2019. Double-blind, randomized pilot clinical trial targeting alpha oscillations with transcranial alternating current stimulation (tACS) for the treatment of major depressive disorder (MDD). Translational Psychiatry 9 (1), 106. doi:10.1038/s41398-019-0439-0.

Andersen, P., Silfvenius, H., Sundberg, S., O. Sveen, H.W., 1978. Functional characteristics of unmyelinated fibres in the hippocampal cortex. Brain Research 144, 11–18. doi:10.1016/0006-8993(78)90431-6.

Angeli, D., Ferrell, J.E., Sontag, E.D., 2004. Detection of multistability, bifurcations, and hysteresis in a large class of biological positive-feedback systems. Proceedings of the National Academy of Sciences 101 (7), 1822–1827. doi:10.1073/pnas.0308265100.

Anticevic, A., Gancsos, M., Murray, J.D., Repovs, G., Driesen, N.R., Ennis, D.J., Niciu, M.J., Morgan, P.T., Surti, T.S., Bloch, M.H., Ramani, R., Smith, M.A., Wang, X.-J., Krystal, J.H., Corlett, P.R., 2012. NMDA receptor function in large-scale anticorrelated neural systems with implications for cognition and schizophrenia. Proceedings of the National Academy of Sciences 109 (41), 16720–16725. doi:10.1073/pnas.1208494109.

Arthur, W.B., 1990. Positive feedbacks in the economy. Scientific American 262 (2), 92–99. doi:10.1038/scientificamerican0290-92.

Attneave, F., 1971. Multistability in perception. Scientific American 225 (6), 62–71. doi:10.1038/scientificamerican1271-62.

Attwell, D., Laughlin, S.B., 2001. An Energy Budget for Signaling in the Grey Matter of the Brain. Journal of Cerebral Blood Flow & Metabolism 21 (10), 1133–1145. doi:10.1097/00004647-200110000-00001.

Avery, D.H., Holtzheimer, P.E., Fawaz, W., Russo, J., Neumaier, J., Dunner, D.L., Haynor, D.R., Claypoole, K.H., Wajdik, C., Roy-Byrne, P., 2006. A Controlled Study of Repetitive Transcranial Magnetic Stimulation in Medication-Resistant Major Depression. Biological Psychiatry 59 (2), 187–194. doi:10.1016/j.biopsych.2005.07.003.

Ayub, R., Sun, K.L., Flores, R.E., Lam, V.T., Jo, B., Saggar, M., Fung, L.K., 2021. Thalamocortical connectivity is associated with autism symptoms in high-functioning adults with autism and typically developing adults. Translational Psychiatry 11 (1), 93. doi:10.1038/s41398-021-01221-0.

Basser, P.J., Pajevic, S., Pierpaoli, C., Duda, J., Aldroubi, A., 2000. In vivo fiber tractography using DT-MRI data. Magnetic Resonance in Medicine 44 (4), 625–632. doi:10.1002/1522-2594(200010)44:4<625::aid-mrm17>3.0.co;2-o.

Berger, H., 1929. Aber das elektrenkephalogramm des menschen. Archiv für Psychiatrie und Nervenkrankheiten 87 (1), 527–570. doi:10.1007/bf01797193.

Bilker, W. B., Hansen, J. A., Brensinger, C. M., Richard, J., Gur, R. E., Gur, R. C., 2012. Development of abbreviated nine-Item forms of the Raven's Standard Progressive Matrices Test. Assessment 19 (3), 352–369. doi:10.1177/1073191112446655.

Bishop, G.H., 1932. Cyclic changes in excitability of the optic pathway of the rabbit. American Journal of Physiology-Legacy Content 103 (1), 213–224. doi:10.1152/ajplegacy.1932.103.1.213.

Bluhm, R., Williamson, P., Lanius, R., Thberge, J., Densmore, M., Bartha, R., Neufeld, R., Osuch, E., 2009. Resting state default-mode network connectivity in early depression using a seed regionofinterest analysis: Decreased connectivity with caudate nucleus. Psychiatry and Clinical Neurosciences 63 (6), 754–761. doi:10.1111/j.1440-1819.2009.02030.x.

Breakspear, M., 2017. Dynamic models of large-scale brain activity. Nature Neuroscience 20 (3), 340–352. doi:10.1038/nn.4497.

Brunoni, A.R., Moffa, A.H., Fregni, F., Palm, U., Padberg, F., Blumberger, D.M., Daskalakis, Z.J., Bennabi, D., Haffen, E., Alonzo, A., Loo, C.K., 2016. Transcranial direct current stimulation for acute major depressive episodes: Meta-analysis of individual patient data. British Journal of Psychiatry 208 (6), 522–531. doi:10.1192/bjp.bp.115.164715.

Cabral, J., Kringelbach, M.L., Deco, G., 2017. Functional connectivity dynamically evolves on multiple time-scales over a static structural connectome: Models and mechanisms. NeuroImage 160, 84–96. doi:10.1016/j.neuroimage.2017.03.045.

Civier, O., Smith, R.E., Yeh, C.-H., Connelly, A., Calamante, F., 2019. Is removal of weak connections necessary for graph-theoretical analysis of dense weighted structural connectomes from diffusion MRI? NeuroImage doi:10.1016/j.neuroimage.2019.02.039.

Cox, R.W., Hyde, J.S., 1997. Software tools for analysis and visualization of fmri data. NMR in Biomedicine 10 (4-5), 171–178. doi:10.1002/(SICI)1099-1492(199706/08)10:4/5<171::AID-NBM453>3.0.CO;2-L.

Damoiseaux, J.S., Greicius, M.D., 2009. Greater than the sum of its parts: a Review of studies combining structural connectivity and resting-state functional connectivity. Brain Structure and Function 213 (6), 525–533. doi:10.1007/s00429-009-0208-6.

Deco, G., Jirsa, V., McIntosh, A.R., Sporns, O., Ktter, R., 2009. Key role of coupling, delay, and noise in resting brain fluctuations. Proceedings of the National Academy of Sciences 106 (25), 10302–10307. doi:10.1073/pnas.0901831106.

Deco, G., Jirsa, V.K., 2012. Ongoing cortical activity at rest: Criticality, multistability, and ghost attractors. Journal of Neuroscience 32 (10), 3366–3375. doi:10.1523/JNEUROSCI.2523-11.2012.

Deco, G., Jirsa, V.K., McIntosh, A.R., 2011. Emerging concepts for the dynamical organization of resting-state activity in the brain. Nature Reviews Neuroscience 12 (1), 43. doi:10.1038/nrn2961.

Deco, G., Jirsa, V.K., McIntosh, A.R., 2013. Resting brains never rest: Computational insights into potential cognitive architectures. Trends in Neurosciences 36 (5), 268–274. doi:10.1016/j.tins.2013.03.001.

Deco, G., Ponce-Alvarez, A., Hagmann, P., Romani, G.L., Mantini, D., Corbetta, M., 2014. How local excitation-inhibition ratio impacts the whole brain dynamics. Journal of Neuroscience 34, 7886–7898. doi:10.1523/jneurosci.5068-13.2014.

Deco, G., Ponce-Alvarez, A., Mantini, D., Romani, G.L., Hagmann, P., Corbetta, M., 2013. Resting-state functional connectivity emerges from structurally and dynamically shaped slow linear fluctuations. Journal of Neuroscience 33, 11239–11252. doi:10.1523/jneurosci.1091-13.2013.

Demirta, M., Burt, J.B., Helmer, M., Ji, J.L., Adkinson, B.D., Glasser, M.F., Essen, D.C.V., Sotiropoulos, S.N., Anticevic, A., Murray, J.D., 2019. Hierarchical heterogeneity across human cortex shapes large-scale neural dynamics. Neuron 101, 1181–1194.e13. doi:10.1016/j.neuron.2019.01.017.

Desikan, R.S., Sgonne, F., Fischl, B., Quinn, B.T., Dickerson, B.C., Blacker, D., Buckner, R.L., Dale, A.M., Maguire, R.P., Hyman, B.T., Albert, M.S., Killiany, R.J., 2006. An automated labeling system for subdividing the human cerebral cortex on MRI scans into gyral based regions of interest. NeuroImage 31 (3), 968–980. doi:10.1016/j.neuroimage.2006.01.021.

Doron, K.W., Bassett, D.S., Gazzaniga, M.S., 2012. Dynamic network structure of interhemispheric coordination. Proceedings of the National Academy of Sciences 109 (46), 18661–18668. doi:10.1073/pnas.1216402109.

Duncan, J., Seitz, R. J., Kolodny, J., Bor, D., Herzog, H., Ahmed, A., Newell, F. N., Emslie, H., 2000. A Neural Basis for General Intelligence. Science 289 (5478), 457–460. doi:10.1126/science.289.5478.457.

Esteban, O., Blair, R., Markiewicz, C.J., Berleant, S.L., Moodie, C., Ma, F., Isik, A.I., Erramuzpe, A., Kent, James, D., Goncalves, M., DuPre, E., Sitek, K.R., Gomez, D.E.P., Lurie, D.J., Ye, Z., Poldrack, R.A., Gorgolewski, K.J., 2018. fmriprep. Software doi:10.5281/zenodo.852659.

Esteban, O., Markiewicz, C., Blair, R.W., Moodie, C., Isik, A.I., Erramuzpe Aliaga, A., Kent, J., Goncalves, M., DuPre, E., Snyder, M., Oya, H., Ghosh, S., Wright, J., Durnez, J., Poldrack, R., Gorgolewski, K.J., 2018. fMRIPrep: a robust preprocessing pipeline for functional MRI. Nature Methods doi:10.1038/s41592-018-0235-4.

Fox, M.D., Snyder, A.Z., Zacks, J.M., Raichle, M.E., 2006. Coherent spontaneous activity accounts for trial-to-trial variability in human evoked brain responses. Nature Neuroscience 9 (1), 23–25. doi:10.1038/nn1616.

Garrity, A.G., Pearlson, G.D., McKiernan, K., Lloyd, D., Kiehl, K.A., Calhoun, V.D., 2007. Aberrant "default mode" functional connectivity in schizophrenia. American Journal of Psychiatry 164 (3), 450–457. doi:10.1176/ajp.2007.164.3.450.

Gerloff, C., Andres, F.G., 2002. Bimanual coordination and interhemispheric interaction. Acta Psychologica 110 (2-3), 161–186. doi:10.1016/s0001-6918(02)00032-x.

Ghosh, A., Rho, Y., McIntosh, A.R., Ktter, R., Jirsa, V.K., 2008. Noise during rest enables the exploration of the brain's dynamic repertoire. PLoS Computational Biology 4 (10). doi:10.1371/journal.pcbi.1000196.

Glasser, M.F., Sotiropoulos, S.N., Wilson, J.A., Coalson, T.S., Fischl, B., Andersson, J.L., Xu, J., Jbabdi, S., Webster, M., Polimeni, J.R., Essen, D.C.V., Jenkinson, M., Consortium, W.-M.H., 2013. The minimal preprocessing pipelines for the Human Connectome Project. NeuroImage 80, 105–124. doi:10.1016/j.neuroimage.2013.04.127.

Golos, M., Jirsa, V., Dauc, E., 2015. Multistability in large scale models of brain activity. PLoS computational biology 11 (12), e1004644. doi:10.1371/journal.pcbi.1004644.

Golubitsky, M., Stewart, 2002. The Symmetry Perspective - From Equilibrium to Chaos in Phase Space and Physical Space. Birkhäuser, Basel doi:10.1007/978-3-0348-8167-8.

Golubitsky, M., Stewart, I., Buono, P.-L., Collins, J.J., 1999. Symmetry in locomotor central pattern generators and animal gaits. Nature 401 (6754), 693–695.

Gordon, E.M., Laumann, T.O., Gilmore, A.W., Newbold, D.J., Greene, D.J., Berg, J.J., Ortega, M., Hoyt-Drazen, C., Gratton, C., Sun, H., Hampton, J.M., Coalson, R.S., Nguyen, A.L., McDermott, K.B., Shimony, J.S., Snyder, A.Z., Schlaggar, B.L., Petersen, S.E., Nelson, S.M., Dosenbach, N.U.F., 2017. Precision functional mapping of individual human brains. Neuron 95 (4), 791–807.e7. doi:10.1016/j.neuron.2017.07.011.

Gorgolewski, K., Burns, C.D., Madison, C., Clark, D., Halchenko, Y.O., Waskom, M.L., Ghosh, S., 2011. Nipype: a flexible, lightweight and extensible neuroimaging data processing framework in python. Frontiers in Neuroinformatics 5, 13. doi:10.3389/fninf.2011.00013.

Gorgolewski, K.J., Esteban, O., Markiewicz, C.J., Ziegler, E., Ellis, D.G., Notter, M.P., Jarecka, D., Johnson, H., Burns, C., Manhes-Savio, A., Hamalainen, C., Yvernault, B., Salo, T., Jordan, K., Goncalves, M., Waskom, M., Clark, D., Wong, J., Loney, F., Modat, M., Dewey, B.E., Madison, C., Visconti di Oleggio Castello, M., Clark, M.G., Dayan, M., Clark, D., Keshavan, A., Pinsard, B., Gramfort, A., Berleant, S., Nielson, D.M., Bougacha, S., Varoquaux, G., Cipollini, B., Markello, R., Rokem, A., Moloney, B., Halchenko, Y.O., Wassermann, D., Hanke, M., Horea, C., Kaczmarzyk, J., de Hollander, G., DuPre, E., Gillman, A., Mordom, D., Buchanan, C., Tungaraza, R., Pauli, W.M., Iqbal, S., Sikka, S., Mancini, M., Schwartz, Y., Malone, I.B., Dubois, M., Frohlich, C., Welch, D., Forbes, J., Kent, J., Watanabe, A., Cumba, C., Huntenburg, J.M., Kastman, E., Nichols, B.N., Eshaghi, A., Ginsburg, D., Schaefer, A., Acland, B., Giavasis, S., Kleesiek, J., Erickson, D., Kttner, R., Haselgrove, C., Correa, C., Ghayoor, A., Liem, F., Millman, J., Haehn, D., Lai, J., Zhou, D., Blair, R., Glatard, T., Renfro, M., Liu, S., Kahn, A.E., Prez-Garca, F., Triplett, W., Lampe, L., Stadler, J., Kong, X.-Z., Hallquist, M., Chetverikov, A., Salvatore, J., Park, A., Poldrack, R., Craddock, R.C., Inati, S., Hinds, O., Cooper, G., Perkins, L.N., Marina, A., Mattfeld, A., Noel, M., Snoek, L., Matsubara, K., Cheung, B., Rothmei, S., Urchs, S., Durnez, J., Mertz, F., Geisler, D., Floren, A., Gerhard, S., Sharp, P., Molina-Romero, M., Weinstein, A., Broderick, W., Saase, V., Andberg, S.K., Harms, R., Schlamp, K.,

Arias, J., Papadopoulos Orfanos, D., Tarbert, C., Tambini, A., De La Vega, A., Nickson, T., Brett, M., Falkiewicz, M., Podranski, K., Linkersdrfer, J., Flandin, G., Ort, E., Shachnev, D., McNamee, D., Davison, A., Varada, J., Schwabacher, I., Pellman, J., Perez-Guevara, M., Khanuja, R., Pannetier, N., McDermottroe, C., Ghosh, S., 2018. Nipype. Software doi:10.5281/zenodo.596855.

Green, T., Saggar, M., Ishak, A., Hong, D.S., Reiss, A.L., 2017. X-Chromosome effects on attention networks: Insights from imaging resting-state networks in Turner Syndrome. Cerebral Cortex 28 (9), 3176–3183. doi:10.1093/cercor/bhx188.

Greve, D.N., Fischl, B., 2009. Accurate and robust brain image alignment using boundary-based registration. NeuroImage 48 (1), 63–72. doi:10.1016/j.neuroimage.2009.06.060.

Griffanti, L., Douaud, G., Bijsterbosch, J., Evangelisti, S., Alfaro-Almagro, F., Glasser, M.F., Duff, E.P., Fitzgibbon, S., Westphal, R., Carone, D., Beckmann, C.F., Smith, S.M., 2017. Hand classification of fMRI ICA noise components. NeuroImage 154, 188–205. doi:10.1016/j.neuroimage.2016.12.036.

Hagmann, P., Cammoun, L., Gigandet, X., Meuli, R., Honey, C.J., Wedeen, V.J., Sporns, O., 2008. Mapping the structural core of human cerebral cortex. PLoS Biology 6 (7), e159. doi:10.1371/journal.pbio.0060159.

Hansen, E.C., Battaglia, D., Spiegler, A., Deco, G., Jirsa, V.K., 2015. Functional connectivity dynamics: Modeling the switching behavior of the resting state. NeuroImage 105 (Cereb. Cortex 2012), 525–535. doi:10.1016/j.neuroimage.2014.11.001.

Harris, J.J., Jolivet, R., Attwell, D., 2012. Synaptic Energy Use and Supply. Neuron 75 (5), 762–777. doi:10.1016/j.neuron.2012.08.019.

van den Heuvel, M.P., Pol, H.E.H., 2010. Exploring the brain network: A review on resting-state fMRI functional connectivity. European Neuropsychopharmacology 20 (8), 519–534. doi:10.1016/j.euroneuro.2010.03.008.

Honey, C.J., Ktter, R., Breakspear, M., Sporns, O., 2007. Network structure of cerebral cortex shapes functional connectivity on multiple time scales. Proceedings of the National Academy of Sciences 104 (24), 10240–10245. doi:10.1073/pnas.0701519104.

Honey, C.J., Sporns, O., Cammoun, L., Gigandet, X., Thiran, J.P., Meuli, R., Hagmann, P., 2009. Predicting human resting-state functional connectivity from structural connectivity. Proceedings of the National Academy of Sciences 106 (6), 2035–2040. doi:10.1073/pnas.0811168106.

Hutchison, R.M., Womelsdorf, T., Allen, E.A., Bandettini, P.A., Calhoun, V.D., Corbetta, M., Penna, S.D., Duyn, J.H., Glover, G.H., Gonzalez-Castillo, J., Handwerker, D.A., Keilholz, S., Kiviniemi, V., Leopold, D.A., Pasquale, F.d., Sporns, O., Walter, M., Chang, C., 2013. Dynamic functional connectivity: Promise, issues, and interpretations. NeuroImage 80, 360–378. doi:10.1016/j.neuroimage.2013.05.079.

Jenkinson, M., Bannister, P., Brady, M., Smith, S., 2002. Improved optimization for the robust and accurate linear registration and motion correction of brain images. NeuroImage 17 (2), 825–841. doi:10.1006/nimg.2002.1132.

Jobst, B.M., Hindriks, R., Laufs, H., Tagliazucchi, E., Hahn, G., Ponce-Alvarez, A., Stevner, A.B.A., Kringelbach, M.L., Deco, G., 2017. Increased Stability and Breakdown of Brain Effective Connectivity During Slow-Wave Sleep: Mechanistic Insights from Whole-Brain Computational Modelling. Scientific Reports 7 (1), 4634. doi:10.1038/s41598-017-04522-x.

Kelso, J.A.S., 1995. Dynamic Patterns: The Self-Organization of Brain and Behavior. The MIT Press, Cambridge, Massachusetts.

Kelso, J.A.S., 2012. Multistability and metastability: Understanding dynamic coordination in the brain. Philosophical Transactions of the Royal Society B: Biological Sciences 367 (1591), 906–918.

Kelso, J.A.S., Dumas, G., Tognoli, E., 2013. Outline of a general theory of behavior and brain coordination. Neural Networks 37, 120–131. doi:10.1016/j.neunet.2012.09.003.

Klein, A., Tourville, J., 2012. 101 Labeled Brain Images and a Consistent Human Cortical Labeling Protocol. Frontiers in Neuroscience 6, 171. doi:10.3389/fnins.2012.00171.

Laumann, T.O., Snyder, A.Z., Mitra, A., Gordon, E.M., Gratton, C., Adeyemo, B., Gilmore, A.W., Nelson, S.M., Berg, J.J., Greene, D.J., McCarthy, J.E., Tagliazucchi, E., Laufs, H., Schlaggar, B.L., Dosenbach, N.U.F., Petersen, S.E., 2016. On the stability of BOLD fMRI correlations. Cerebral Cortex 27 (10), 4719–4732. doi:10.1093/cercor/bhw265.

Laurent, M., Kellershohn, N., 1999. Multistability: a major means of differentiation and evolution in biological systems. Trends in Biochemical Sciences 24 (11), 418–422. doi:10.1016/S0968-0004(99)01473-5.

Ligeois, R., Li, J., Kong, R., Orban, C., Ville, D.V.D., Ge, T., Sabuncu, M.R., Yeo, B.T.T., 2019. Resting brain dynamics at different timescales capture distinct aspects of human behavior. Nature Communications 10 (1), 2317. doi:10.1038/s41467-019-10317-7.

Murray, J.D., Anticevic, A., Gancsos, M., Ichinose, M., Corlett, P.R., Krystal, J.H., Wang, X.-J., 2014. Linking microcircuit dysfunction to cognitive impairment: Effects of disinhibition associated with schizophrenia in a cortical working memory model. Cerebral Cortex 24 (4), 859–872. doi:10.1093/cercor/bhs370.

Orser, B.A., Pennefather, P.S., MacDonald, J.F., 1997. Multiple mechanisms of ketamine blockade of N-methyl-D-aspartate receptors. Anesthesiology 86 (4), 903–917. doi:10.1097/00000542-199704000-00021.

Park, H.-J., Friston, K., 2013. Structural and functional brain networks: from Connections to cognition. Science 342 (6158), 1238411. doi:10.1126/science.1238411.

Pillai, A.S., Jirsa, V.K., 2017. Symmetry breaking in space-time hierarchies shapes brain dynamics and behavior. Neuron 94 (5), 1010–1026. doi:10.1016/j.neuron.2017.05.013.

Ponce-Alvarez, A., He, B.J., Hagmann, P., Deco, G., 2015. Task-Driven Activity Reduces the Cortical Activity Space of the Brain: Experiment and Whole-Brain Modeling. PLOS Computational Biology 11 (8), e1004445. doi:10.1371/journal.pcbi.1004445.

Power, J.D., Mitra, A., Laumann, T.O., Snyder, A.Z., Schlaggar, B.L., Petersen, S.E., 2014. Methods to detect, characterize, and remove motion artifact in resting state fmri. NeuroImage 84 (Supplement C), 320–341. doi:10.1016/j.neuroimage.2013.08.048.

Raichle, M.E., Mintun, M.A., 2006. Brain work and brain imaging. Annual Review of Neuroscience 29 (1), 449–476. doi:10.1146/annurev.neuro.29.051605.112819.

Saggar, M., Uddin, L.Q., 2019. Pushing the boundaries of psychiatric neuroimaging to ground diagnosis in biology. eNeuro, ENEURO.0384 19.2019 doi:10.1523/eneuro.0384-19.2019.

Schöner, G., Kelso, J.A.S., 1988. Dynamic pattern generation in behavioral and neural systems. Science 239 (4847), 1513–1520. doi:10.1126/science.3281253.

Schroeder, C.E., Lakatos, P., 2009. Low-frequency neuronal oscillations as instruments of sensory selection. Trends in Neurosciences 32 (1), 9–18. doi:10.1016/j.tins.2008.09.012.

Smith, R.E., Tournier, J.-D., Calamante, F., Connelly, A., 2012. Anatomically-constrained tractography: Improved diffusion MRI streamlines tractography through effective use of anatomical information. NeuroImage 62 (3), 1924–1938. doi:10.1016/j.neuroimage.2012.06.005.

Smith, R.E., Tournier, J.-D., Calamante, F., Connelly, A., 2015. SIFT2: Enabling dense quantitative assessment of brain white matter connectivity using streamlines tractography. NeuroImage 119, 338–351. doi:10.1016/j.neuroimage.2015.06.092.

Smith, S.M., Beckmann, C.F., Andersson, J., Auerbach, E.J., Bijsterbosch, J., Douaud, G., Duff, E., Feinberg, D.A., Griffanti, L., Harms, M.P., Kelly, M., Laumann, T., Miller, K.L., Moeller, S., Petersen, S., Power, J., Salimi-Khorshidi, G., Snyder, A.Z., Vu, A.T., Woolrich, M.W., Xu, J., Yacoub, E., Uurbil, K., Essen, D.C.V., Glasser, M.F., Consortium, W.-M.H., 2013. Resting-state fMRI in the Human Connectome Project. NeuroImage 80, 144–168. doi:10.1016/j.neuroimage.2013.05.039.

Somogyi, P., Tams, G., Lujan, R., Buhl, E.H., 1998. Salient features of synaptic organisation in the cerebral cortex. Brain Research Reviews 26 (2), 113–135. doi:10.1016/S0165-0173(97)00061-1.

Sporns, O., 2002. Network analysis, complexity, and brain function. Complexity 8 (1), 56–60. doi:10.1002/cplx.10047.

Sporns, O., 2004. Complex neural dynamics. Springer Berlin Heidelberg, Berlin, Heidelberg, pp. 197–215.

Sporns, O., 2011. The human connectome: a Complex network. Annals of the New York Academy of Sciences 1224 (1), 109–125. doi:10.1111/j.1749-6632.2010.05888.x.

Sporns, O., Tononi, G., 2001. Classes of network connectivity and dynamics. Complexity 7 (1), 28–38. doi:10.1002/cplx.10015.

Tognoli, E., Kelso, J., 2014. The metastable brain. Neuron 81 (1), 35–48. doi:10.1016/j.neuron.2013.12.022.

Tournier, J.-D., Calamante, F., Connelly, A., 2010. Improved probabilistic streamlines tractography by 2 order integration over fibre orientation distributions. In: Proceedings of the 18th Annual Meeting of ISMRM (International Society for Magnetic Resonance in Medicine), p. 1670.

Van Essen, D.C., Smith, S.M., Barch, D.M., Behrens, T.E., Yacoub, E., Ugurbil, K., Consortium, f.t.W.-M.H., 2013. The WU-Minn Human Connectome Project: An overview. NeuroImage 80, 62–79. doi:10.1016/j.neuroimage.2013.05.041.

Verma, A., Moghaddam, B., 1996. NMDA receptor antagonists impair prefrontal cortex function as assessed via spatial delayed alternation performance in rats: Modulation by dopamine. Journal of Neuroscience 16 (1), 373–379. doi:10.1523/jneurosci.16-01-00373.1996.

Wang, M., Wong, A.H., Liu, F., 2012. Interactions between NMDA and dopamine receptors: a Potential therapeutic target. Brain research 1476, 154–163. doi:10.1016/j.brainres.2012.03.029.

Wang, X.-J., 2002. Probabilistic decision making by slow reverberation in cortical circuits. Neuron 36, 955–968. doi:10.1016/s0896-6273(02)01092-9.

Wilson, H.R., Cowan, J.D., 1972. Excitatory and inhibitory interactions in localized populations of model neurons. Biophysical Journal 12, 1–24. doi:10.1016/s0006-3495(72)86068-5.

Wilson, H.R., Cowan, J.D., 1973. A mathematical theory of the functional dynamics of cortical and thalamic nervous tissue. Kybernetik 13, 55–80. doi:10.1007/bf00288786.

Wong, K.-F., Wang, X.-J., 2006. A recurrent network mechanism of time integration in perceptual decisions. Journal of Neuroscience 26 (4), 1314–1328. doi:10.1523/jneurosci.3733-05.2006.

Yeomans, J.S., 1979. The absolute refractory periods of self-stimulation neurons. Physiology & Behavior 22, 911–919. doi:10.1016/0031-9384(79)90336-6.

Zhang, D., Raichle, M.E., 2010. Disease and the brain's dark energy. Nature Reviews Neurology 6 (1), 15–28. doi:10.1038/nrneurol.2009.198.

Zhang, M., Beetle, C., Kelso, J.A.S., Tognoli, E., 2019. Connecting empirical phenomena and theoretical models of biological coordination across scales. Journal of The Royal Society Interface 16 (157), 20190360. doi:10.1098/rsif.2019.0360.

Zhang, M., Riddle, J., Frohlich, F., 2022. Closed-loop control of bistable symptom states. Brain Stimulation doi:10.1016/j.brs.2022.02.010.

Supplementary Materials for "Cross-attractor repertoire provides new perspective on structure-function relationship in the brain" by Zhang, Sun, & Saggar

S1 Region indices and names

abbreviation	region name	right index	left index
ENT	Entorhinal cortex	1	66
PARH	Parahippocampal cortex	2	65
TP	Temporal pole	3	64
FP	Frontal pole	4	63
FUS	Fusiform gyrus	5	62
TT	Transverse temporal cortex	6	61
LOCC	Lateral occipital cortex	7	60
SP	Superior parietal cortex	8	59
IT	Inferior temporal cortex	9	58
IP	Inferior parietal cortex	10	57
SMAR	Supramarginal gyrus	11	56
BSTS	Bank of the superior temporal sulcus	12	55
MT	Middle temporal cortex	13	54
ST	Superior temporal cortex	14	53
PSTC	Postcentral gyrus	15	52
PREC	Precentral gyrus	16	51
CMF	Caudal middle frontal cortex	17	50
POPE	Pars opercularis	18	49
PTRI	Pars triangularis	19	48
RMF	Rostral middle frontal cortex	20	47
PORB	Pars orbitalis	21	46
LOF	Lateral orbitofrontal cortex	22	45
CAC	Caudal anterior cingulate cortex	23	44
RAC	Rostral anterior cingulate cortex	24	43
SF	Superior frontal cortex	25	42
MOF	Medial orbitofrontal cortex	26	41
LING	Lingual gyrus	27	40
PCAL	Pericalcarine cortex	28	39
CUN	Cuneus	29	38
PARC	Paracentral lobule	30	37
ISTC	Isthmus of the cingulate cortex	31	36
PCUN	Precuneus	32	35
PC	Posterior cingulate cortex	33	34

Table S1: **Names and indices of brain regions**. As in [1], the brain is parcellated into 66 regions as shown in Figure 1b. Here is a list of the specific region names corresponding to each region index. Region 1-33 are on the right hemisphere, and region 66-34 are the homologous regions on the the left hemisphere.

S2 Relation to the Wilson-Cowan model

Formally, the above model can be considered a special variant of the Wilson-Cowan model [2, 3]. Though the specific interpretation of certain parameters differ, the two models describe similar dynamic mechanisms of population-level interaction. The Wilson-Cowan model, in its initial form [2], concerns the dynamics of a pair of interacting excitatory and inhibitory neuronal populations. The activities

of the two populations are denoted as $E(t)$ and $I(t)$—the proportion of firing excitatory/inhibitory cells averaged over a period of time (the refectory period). The model takes the form

$$\tau_E \frac{\mathrm{d}\,E}{\mathrm{d}\,t} = -E + (k_E - r_E E)\mathscr{S}_E(c_1 E - c_2 I + P) \tag{S1}$$

$$\tau_I \frac{\mathrm{d}\,I}{\mathrm{d}\,t} = -I + (k_I - r_I I)\mathscr{S}_I(c_3 E - c_4 I + Q). \tag{S2}$$

τ_E and τ_I are time constants of the dynamics of the excitatory and inhibitory population respectively. $c_\bullet$'s are the coupling parameters between the two population. Coefficients $k_\bullet$ and $r_\bullet$ result from a temporal coarse-graining procedure in the initial derivation (see [2] for detail). $\mathscr{S}_\bullet$ is a sigmoidal transfer function, rising monotonically from 0 to 1 with non-negative input. P and Q are external inputs to their respective populations. If we divide both sides of equation S1-S2 by the time constants, we are looking at the same general form as equation 1-2.

The main difference is between the respective transfer functions. Wilson and Cowan [2] chose a particular form of $\mathscr{S}$ for mathematical analysis:

$$\mathscr{S}(x) = \frac{1}{1 + \exp\left[-a(x-\theta)\right]} - \frac{1}{1 + \exp(a\theta)}, \tag{S3}$$

where parameter a determines the maximum slope of the function $\mathscr{S}$ and parameter θ the location of the maximum slope. Technically, Wilson and Cowan [2] only requires $\mathscr{S}$ to be of a general sigmoidal form. It may reflect the average response of a population of neurons with heterogeneous firing thresholds or heterogeneous afferent connections. The distribution of the said thresholds or connections is reflected in the parameters a and θ.

In other words, the choice of the transfer function and the parameters is *non-specific* to a predefined microscopic model. Moreover, Wilson and Cowan [2] took a function-oriented approach to analyzing the model. The key was whether the model was able to produce fundamental behaviors expected from a neural model—multistability, hysteresis, and oscillation—for *some* specific choice of parameters and transfer function. Qualitative conclusions from their analysis depend on the general geometric properties of the transfer function rather than the specific form of equation S3.

The transfer function of the present model (equation 3) follows the general geometric properties assumed by Wilson and Cowan [2]. The difference is that the parameters in equation 3 are associated specifically with a microscopic model [4], a network of leaky integrate-and-fire neurons with biologically plausible parameters, as inherited from the reduced Wong-Wang model [5, 6]. This choice provides a channel of correspondence between parameters of the models at different scales of description. To expand on this point, we next elaborate on the connection between the present model and the reduced Wong-Wang model.

S3 Relation to the reduced Wong-Wang model

The present model is also a variant of the Wong-Wang model [5] and its high-dimensional generalizations, here referred to as the reduced Wong-Wang model [1, 6, 7]. In particular, we consider the model of whole-brain dynamics [6, 7],

$$\frac{\mathrm{d}\,S_E^{(i)}(t)}{\mathrm{d}\,t} = -\frac{S_E^{(i)}}{\tau_E} + \left(1 - S_E^{(i)}\right)\gamma_E \tilde{H}_E\left(w_{EE}^{(i)} S_E^{(i)} - w_{IE}^{(i)} S_I^{(i)} + I_G^{(i)}(\vec{S}_E)\right) + \sigma\xi^{(i)}(t) \tag{S4}$$

$$\frac{\mathrm{d}\,S_I^{(i)}(t)}{\mathrm{d}\,t} = -\frac{S_I^{(i)}}{\tau_I} + \tilde{H}_I\left(w_{EI}^{(i)} S_E^{(i)} - w_{II}^{(i)} S_I^{(i)} + I_I\right) + \sigma\xi^{(i)}(t), \tag{S5}$$

following the same notations as in equation 4-6, where

$$\tilde{H}_p(x) = \frac{a_p x - b_p}{1 - e^{-d_p(a_p x - b_p)}} \tag{S6}$$

with $p \in \{E, I\}$ denoting the excitatory and the inhibitory population respectively. The parameters a_p, b_p and d_p were chosen such that $\tilde{H}_p$ approximates the average firing rate of an ensemble of leaky integrate-and-fire neurons receiving uncorrelated noisy inputs.

More specifically, the sub-threshold dynamics of the membrane potential $V(t)$ of each neuron can be described as

$$C_m \frac{\mathrm{d}\, V(t)}{\mathrm{d}\, t} = -g_L \left(V(t) - V_L\right) + I_{syn}(t) \tag{S7}$$

where C_m is the membrane capacitance, g_L the leak conductance, and V_L the resting potential of the membrane. The total synaptic input current $I_{syn}(t)$ is a random process with an average μ_C and standard deviation σ_C. When $V(t)$ reaches a threshold V_{th}, the neuron emits a spike after which the membrane potential returns to a reset voltage V_{reset} and stays there for a duration τ_{ref}, i.e. the refractory period.

The average firing rate ν of an ensemble of such neurons can be derived from the Fokker-Planck approximation that describes the evolution of the membrane voltage distribution of an ensemble of neurons (see e.g. [8, Section 1], [9] for descriptions of the Fokker-Planck approach). This eventually leads to the first-passage time equation (average time for crossing the threshold),

$$\nu = \left(\tau_{\mathrm{ref}} + \tau_m \sqrt{\pi} \int_{\frac{V_{\mathrm{reset}} - V_{\mathrm{ss}}}{\sigma_V}}^{\frac{V_{\mathrm{th}} - V_{\mathrm{ss}}}{\sigma_V}} e^{x^2} (1 + \mathrm{erf}(x)) dx \right)^{-1} \tag{S8}$$

where $\tau_m = C_m / g_L$ is the membrane time constant, $\sigma_V = \sqrt{\tau_m} \sigma_C / C_m$ the standard deviation of the depolarization, $\mathrm{erf}(x)$ the error function

$$\mathrm{erf}(x) = \frac{2}{\sqrt{\pi}} \int_0^x e^{-u^2} du, \tag{S9}$$

and V_{ss} the steady state voltage

$$V_{\mathrm{ss}} = V_L + \frac{I_{syn}}{g_L}. \tag{S10}$$

The transfer function employed by Wong and Wang [5, 10], i.e. equation S6 with appropriate choice of parameters, is a good approximation of equation S8 when the input level is low.

Thus, the first passage equation S8 provides a bridge between the transfer function (equation S6) and the single-cell level model (equation S7) incorporating realistic biophysical parameters (Table S2). In other words, it allows one to use empirically measurable quantities at the neuronal level to directly constrain the the transfer function and the entire model. This is a major difference with the Wilson-Cowan model [2, 3].

parameter	interpretation	value
C_m	membrane capacitance	0.5, 0.2 (nF)
g_L	leak conductance	25, 20 (nS)
τ_m	membrane time constant	20, 10 (ms)
τ_{ref}	refractory period	2 (ms)
V_L	resting membrane potential	-70 (mV)
V_{th}	threshold for firing	-50 (mV)
V_{reset}	reset potential	-55 (mV)

Table S2: **Biophysical parameters of a single leaky-integrate-and-fire neuron.** If two parameter values are provided in the right column, the first value is for a generic pyramidal cell and the second is for a generic interneuron. Differences between the biophysical parameters of different cell types lead to differences in the transfer functions (equation S6).

According to the first passage equation S8, the firing rate ν is a sigmoidal function of the input, which saturates at $r_{max} \equiv 1/\tau_{ref}$. This is not the case, however, for the transfer function $\tilde{H}$ (equation S6).

To make the transfer function a better approximation of the first passage equation and at the same time retain the mapping between their parameters, we can simply convert the transfer function by substituting the numerator of $\tilde{H}$ as below

$$H_p(x) = \frac{r_{max} - \tilde{H}_p(r_{max} - x)}{1 - e^{-d_p(a_p x - b_p)}}. \tag{S11}$$

Thus, we obtain the transfer function used in the present model (equation 3). H_p matches $\tilde{H}_p$ for low levels of input but flattens out eventually at r_{max} as one would expect from equation S8.

In short, the present model is endowed with the geometric properties of the Wilson-Cowan model [2, 3] and at the same time consistent with the neuronal level-to-population level mapping of the reduced Wong-Wang model [5, 6].

S4 Local structural connectivity controls dynamic repertoire of an isolated brain region

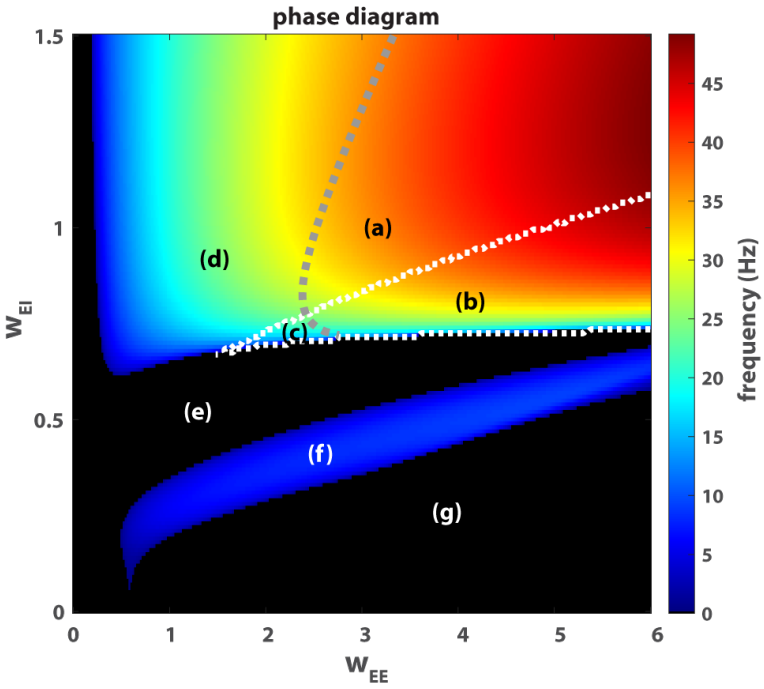

Figure S1: **Local dynamics controlled by the strength of excitatory-to-excitatory connection w_{EE} and excitatory-to-inhibitory connection w_{EI}.** (a)-(g) are seven different dynamic regimes of the local model (equation 1-2) in the 2-dimensional parameters space (w_{EE}, w_{EI}). Here the local inhibitory-to-excitatory connectivity w_{IE}—the inhibitory feedback—is matched to the excitatory-to-excitatory connectivity, i.e. $w_{IE} = w_{EE}$; and $I_E = 0.382$ as in [6]. Black areas (e, g) are the regimes of stable equilibrium. Colored areas are the oscillatory regimes: (a)-(b) for limit cycles and (c), (d), (f) for damped oscillations. The color reflects the frequency of oscillation. A gray dashed line indicates the Hopf bifurcation. The triangular area enclosed by white dashed lines (saddle-node bifurcation) is the bi-stable regime (b, c). A typical phase portrait from each regime is provided in Figure S2.

The local model exhibits a rich repertoire of dynamical features, including multistability (b, c in Figure S1, S2), damped oscillation (c, d, f), and limit cycles (sustained oscillation; a, b). Mathematical analysis of the local model (Section S8 in Supplementary Materials for "Cross-attractor repertoire provides new perspective on structure-function relationship in the brain" by Zhang, Sun, & Saggar) shows that nonlinearity in the dynamics can essentially be controlled by two local structural properties: the strength of excitatory-to-excitatory connection w_{EE} and the strength of the excitatory-to-inhibitory connection w_{EI}. Geometrically, the two structural properties "twist" the nullclines (dashed lines in Figure S2). Specifically, stronger w_{EE} introduces a deeper twist and fold of the red nullcline (compare Figure S2a and d), whereas stronger w_{EI} introduces a more vertical twist of the blue nullcline (compare Figure S2d and e). These twists are the key sources of dynamic complexity—multistability and oscillation. For example, when w_{EE} is sufficiently large (equation S30), multistability becomes possible: the folded red nullcline allows for multiple intersections with the blue nullcline, and potentially a greater number of attractors (compare Figure S2c to a; see analytical results in Section S8: Multistability). When w_{EI} is sufficiently large (equation S38), oscillatory activity becomes

possible (analytical results in Section S8: Oscillation). Moreover, the combination of large w_{EE} and w_{EI} gives rise to sustained oscillation (equation S61). The characteristic frequency of such oscillation further depends on the specific values of w_{EE} and w_{EI}. Note that the general qualitative effects of these two local structural properties are consistent with those of the Wilson-Cowan model, but the specific boundaries at which transitions occur are determined by the biophysical constraints inherited from the reduced Wong-Wang model (see equations S38, S61). Analytical results (Section S8) provide detailed quantification of how these boundaries are shifted by different local structural properties.

To maintain a sufficient twist in the red nullcline (red dashed line in Figure S2) and associated multistability and oscillation, inhibitory-to-excitatory feedback w_{IE} needs to be proportional to self-excitation w_{EE} (c.f. equation S20). In the present study, we simply let $w_{IE} = w_{EE}$. This equality is a simpler alternative to the Feedback Inhibition Control adopted in [6] in both numerical and mathematical analyses.

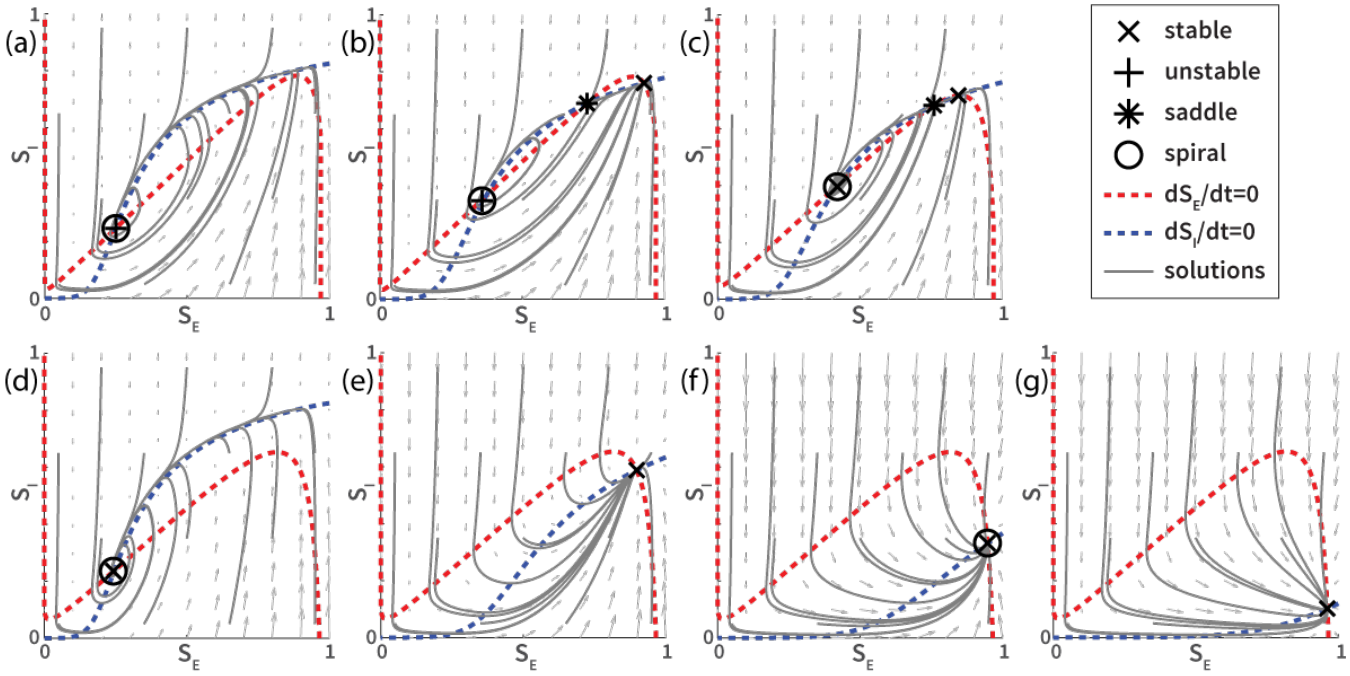

Figure S2: **Example phase portraits from different regimes of the local model**. Phase portraits (a) to (g) are examples chosen from the corresponding regimes in Figure S1. The specific parameters defining local structural connectivity are (a) $w_{EE} = 4$, $w_{EI} = 1$; (b) $w_{EE} = 4$, $w_{EI} = 0.8$; (c) $w_{EE} = 2.3$, $w_{EI} = 0.75$; (d) $w_{EE} = 1.5$, $w_{EI} = 1$; (e) $w_{EE} = 1.5$, $w_{EI} = 0.5$; (f) $w_{EE} = 1.5$, $w_{EI} = 0.3$; (g) $w_{EE} = 1.5$, $w_{EI} = 0.2$. The vector fields (arrows) reflect the underlying dynamics at different points in the state space. Gray trajectories following the vector fields are solutions of the local model (equation 1, 2) given a fixed sets of ten different initial conditions. Nullclines (dashed lines) indicate where the flow of the dynamics is either purely vertical (red) or purely horizontal (blue). The intersections between the nullclines are the fixed points. Different types of fixed points are labeled with different markers (see legend). A fixed point is stable ($\times$) if nearby trajectories converge to it over time, unstable ($+$) if nearby trajectories diverge from it, or a saddle ($*$) if nearby trajectories approach it in some direction(s) but diverge from it in some other direction(s). A fixed point is said to be a spiral ($\circ$) if trajectories near the fixed point rotate either towards the fixed point (damped oscillation) or away from the fixed point (sustained oscillation or limit cycle in the present case). Strong oscillation mainly appears on the ascending branch of the red nullcline. Overall, we see that local connectivity defines the dynamics in each regime essentially by controlling the geometry of the nullclines.

S5 The effects of nonlinearity in the local model

Before getting into the global model, we briefly demonstrate numerically how the present unified model (equation 1-2) extends the reduced Wong-Wang model [5, 6] to more complex scenarios. As expected, the dynamics of the present model match that of the reduced Wong-Wang model for low levels of excitation, i.e. weak local excitatory connectivity (Figure S3a-b). In a regime of stronger local excitatory connectivity, as explored in [7], the two models diverge (Figure S3c-d). In the present model (Figure S3c), all trajectories are well-confined within a physiologically plausible range—state variables S_E and S_I denote the fraction of open channels, which by definition are between 0 and 1. In contrast, certain trajectories of the reduced Wong-Wang model (Figure S3d) overshoot beyond the physiologically plausible range. The effect of added nonlinearity in the present model manifests through the

curvature of the blue nullclines, which confines the flow of oscillatory activities and creates extended multistability (see e.g. Figure S2b). Thus, the present model is more suitable for studying key nonlinear dynamical features in the resting brain.

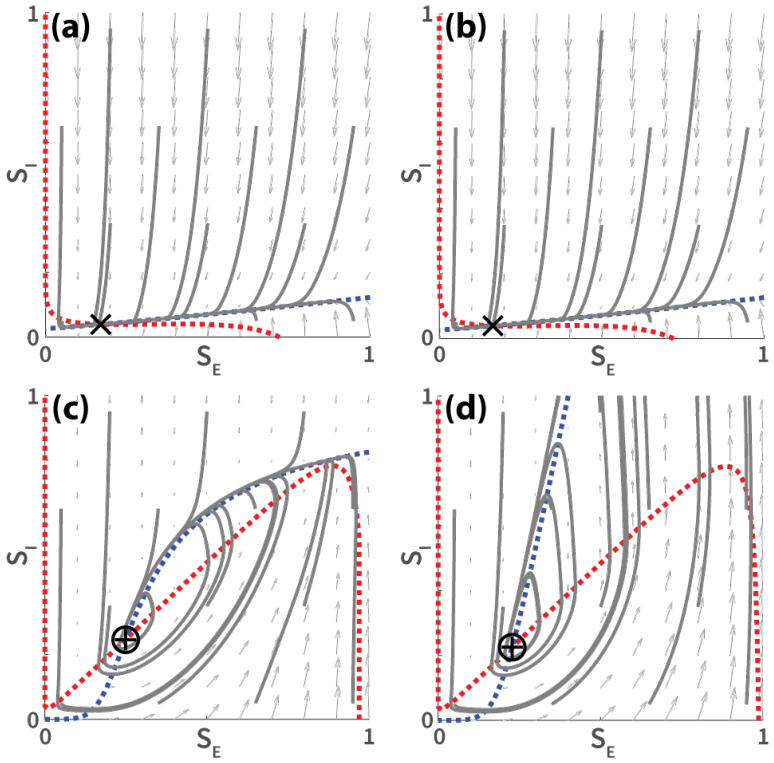

Figure S3: **Comparisons between the present unified model (a, c) and the reduced Wong-Wang model (b, d) in two dynamic regimes.** (a) and (b) show the phase portraits of the present model (equations 1-2) and the reduced Wong-Wang model (equations S4-S5) respectively in a regime of weak local excitatory connectivity. Parameter values are obtained from [6] and identical across the two models: $w_{EE} = 0.21$, $w_{EI} = 0.15$, $w_{IE} = 1$, $w_{II} = 1$, $I_E = 0.382$ and $I_I = 0.267$ (unspecified parameters follow Table 1). The resulted dynamics are virtually identical. (c) and (d) show a similar comparison between the two models in an oscillatory regime, where the local excitatory connectivity is stronger ($w_{EE} = 4$, $w_{EI} = 1$). While the dynamics of the present model (c) is well confined within a realistic range (S_E, $S_I \in [0, 1]$), it is not the case for the reduced Wong-Wang model (d).

S6 Computation of BOLD signal and low-frequency power

In the present study, we are interested in not only the high-frequency activity measurable by, for example, EEG recordings but also low-frequency fluctuations that are often a subject of investigation in fMRI studies. Therefore, we simulated the BOLD activities induced by the underlying neural dynamics and examine their low-frequency properties.

BOLD (Blood-oxygen-level-dependent) activities are computed using the Balloon-Windkessel model [11–14]. The hemodynamic response of the i^{th} brain area takes

the form

$$\dot{s}_i = z_i - \kappa_i s_i - \gamma_i(f_i - 1) \tag{S12}$$

$$\dot{f}_i = s_i \tag{S13}$$

$$\tau_i \dot{v}_i = f_i - v_i^{1/\alpha} \tag{S14}$$

$$\tau_i \dot{q}_i = \frac{f_i}{\rho_i}[1 - (1-\rho_i)^{1/f_i}] - v_i^{1/\alpha - 1} q_i \tag{S15}$$

$$BOLD_i = V_0[k_1(1-q_i) + k_2(1 - q_i/v_i) + k_3(1 - v_i)] \tag{S16}$$

where the interpretation and value of the parameters are given in Table S3. The initial condition is

$$[s_i(0), f_i(0), v_i(0), q_i(0)] = [0, 1, 1, 1] \tag{S17}$$

which is a hemodynamic equilibrium state without neural activity. $z_i(t)$ is the simulated neural activity, corresponding to the gating variable of the excitatory populations $S_E^{(i)}(t)$.

parameter	**interpretation**	**value**
z_i	neuronal activity	$S_E^{(i)}$
s_i	vasodilatory signal	variable
f_i	blood inflow	variable
v_i	blood volume	variable
q_i	deoxyhemoglobin content	variable
κ_i	rate of signal decay	$0.65(s^{-1})$
γ_i	rate of flow-dependent elimination	$0.41(s^{-1})$
τ_i	hemodynamic transit time	0.98 (s)
α	Grubb's exponent	0.32
ρ	resting oxygen extraction fraction	0.34
V_0	resting blood volume fraction	0.02
k_1	BOLD weight parameter	$7\rho_i$
k_2	BOLD weight parameter	2
k_3	BOLD weight parameter	$2\rho_i - 0.2$

Table S3: Parameters of the Balloon-Windkessel model of BOLD activities, obtained from [14].

The power spectrum for each simulated BOLD time series is computed using Welch's method [15], after being subsampled at 720ms intervals (matching the TR of resting state fMRI used in the Human Connectome Project [16]). The full power spectrum $P(\omega)$ was first normalized such that

$$\int_0^{\omega_N} P(\omega)\,\mathrm{d}\,\omega = 1 \tag{S18}$$

where ω_N is the Nyquist frequency (approximately 0.7 Hz for the chosen sampling interval). The low-frequency power is defined as

$$p_\ell = \int_{0.01}^{0.1} P(\omega)\,\mathrm{d}\,\omega. \tag{S19}$$

S7 Discretization of regional states

Although the dynamic landscape of the global model can be quite complex (Figure 4g-i), each region in the globally connected network still falls into discrete states (Figure S4) very much like in the local model (disconnected stripes in Figure 4a-c)—it is the combination of regional states that produces a great variety of attractors at

the global level. Discretized regional states (number on black disks in Figure S4) thus give rise to discretized attractors in the global model. Rank correlation (Spearman) between regional states across these discretized attractors are used to quantify *cross-attractor coordination* in the model brain (Figure 5b in the main text). Using discretized attractors, we quantify how much two regions move up and down together across attractors without considering the distance between the attractors. The distance between attractors are considered separately as the energy cost that constrains such transitions (Figure 6 in the main text).

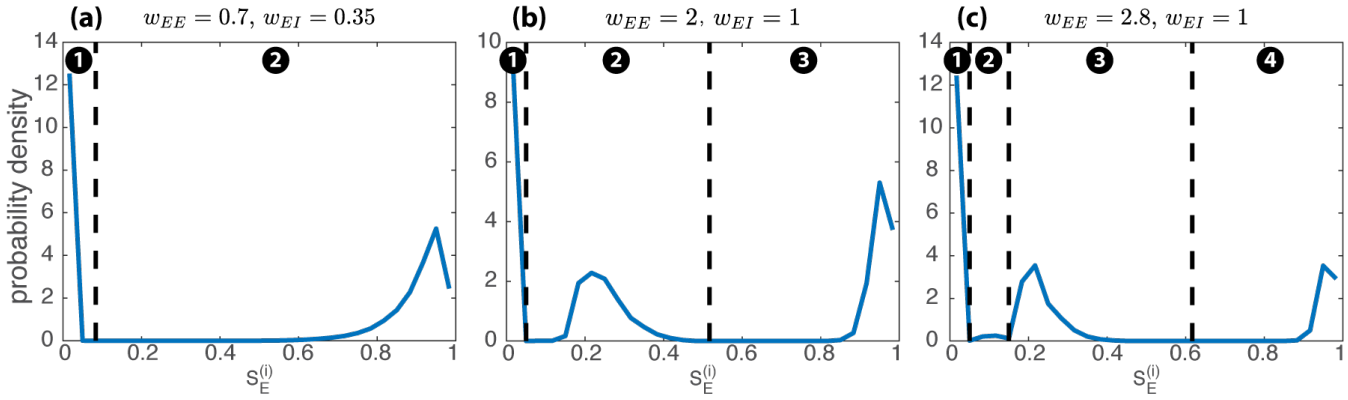

Figure S4: **Brain regions fall into discrete states in the global model**. Blue curves in (a-c) show the distribution of the state of individual brain regions ($S_E^{(i)}$ for any i) in the attractors in the bifurcation diagrams (Figure 4g-i) respectively. Black dashed lines indicate the location of local minima in the distributions. These minima are used to discretize the continuous variable $S_E^{(i)}$ into integer-indexed (discrete) states (number in black disks).

S8 Analysis of the local model

We can see from the numerical analysis that the nullclines (dashed lines in Figure S2) crucially constraint the dynamics of the local model (equation 1-3). Here we take a closer look at their shapes. Red nullcline indicates where there is only vertical flow,

$$\begin{aligned}
&\frac{\mathrm{d}\,S_E}{\mathrm{d}\,t} = 0 \\
\Rightarrow &-\frac{S_E}{\tau_E} + (1 - S_E)\gamma_E\, H_E(w_{EE}S_E - w_{IE}S_I + I_E) = 0 \\
\Rightarrow &S_I = f(S_E) = \frac{w_{EE}}{w_{IE}}S_E - \frac{1}{w_{IE}}H_E^{-1}\left(\frac{S_E}{\tau_E\gamma_E(1 - S_E)}\right) + \frac{I_E}{w_{IE}},
\end{aligned} \tag{S20}$$

and blue nullcline indicates where there is only horizontal flow,

$$\begin{aligned}
&\frac{\mathrm{d}\,S_I}{\mathrm{d}\,t} = 0 \\
\Rightarrow &-\frac{S_I}{\tau_I} + (1 - S_I)\gamma_I\, H_I(w_{EI}S_E - w_{II}S_I + I_I) = 0 \\
\Rightarrow &S_E = g(S_I) = \frac{w_{II}}{w_{EI}}S_I + \frac{1}{w_{EI}}H_I^{-1}\left(\frac{S_I}{\tau_I\gamma_I(1 - S_I)}\right) - \frac{I_I}{w_{EI}}.
\end{aligned} \tag{S21}$$

What is common between the two nullcines, $S_I = f(S_E)$ and $S_E = g(S_I)$, is that their shape crucially depends on a linear term S_p and the inverse of the transfer function H_p^{-1} for $p \in \{E, I\}$. Both terms are monotonically increasing with S_p ($H_p^{-1}(\bullet)$ and $S_p/(1 - S_p)$ are both monotonically increasing function; so is their composition). H_p^{-1} is only defined on a domain between 0 and r_{max}, for which the nullclines are confined within the interval

$$\left[0, 1 - \frac{1}{r_{max}\tau_p\gamma_p}\right]. \tag{S22}$$

Within this interval $S_I = f(S_E)$ (equation S20; red nullcline), overall, goes down from $+\infty$ to $-\infty$, while $S_E = g(S_I)$ (equation S21; blue nullcline) goes up from $-\infty$ to $+\infty$. This results from the dominant effect of H_p^{-1} for a very large or very small input.

In between these extremes, the effect of the linear term is more pronounced. This is especially the case for $S_I = f(S_E)$ (red nullcline): the linear term monotonically increases with S_E, counteracting the descending trend of $-H_E^{-1}$. Given a sufficiently strong excitatory-to-excitatory connection w_{EE} (self-excitation), the linear term "twists" the nullcline counterclockwise, creating an ascending branch in the middle. If we balance the level of self-excitation with inhibitory-feedback—let $w_{EE} = w_{IE}$—equation S20 becomes

$$S_I = f(S_E) = S_E - \frac{1}{w_{EE}} H_E^{-1}\left(\frac{S_E}{\tau_E \gamma_E (1 - S_E)}\right) + \frac{I_E}{w_{EE}}. \tag{S23}$$

In this simplified case, increasing self-excitation w_{EE} reduces the influence of H_E^{-1} such that the slope of middle branch approaches 1.

For $S_E = g(S_I)$ (equation S21), the linear term and the H_I^{-1} term increase together, so that $S_E = g(S_I)$ (blue nullcline) is always monotonically increasing. Given a fixed w_{II}, $S_E = g(S_I)$ increases with S_I at an overall slower rate for larger w_{EI}, or more conveniently seen as $S_I = g^{-1}(S_E)$ increasing faster with S_E for larger w_{EI}. Intuitively, increasing w_{EI} twists $S_E = g(S_I)$ counterclockwise, seen as the middle segment of the blue nullcline becoming more vertical.

We have discussed above how local connectivity w_{EE} and w_{EI} influence the gross geometry of the nullclines—twisting the middle segment of the curve counterclockwise. But how are these geometric changes going to affect the dynamics? We show below that they critically control the multistability and oscillation in the local model.

Multistability. For the local model to be multistable, $S_I = f(S_E)$ (red nullcline) must have an ascending branch, i.e. $f(S_E)$ cannot be monotonically decreasing.

Proof. Suppose that $f(x)$ and $g^{-1}(x)$ are monotonic functions for $x \in [0, 1]$. Specially, $g^{-1}(x)$ is monotonically increasing; $f(x)$ is monotonically decreasing. Assume that $f(x)$ and $g^{-1}(x)$ intersect at two points $x_1 \leqslant x_2$, i.e. $f(x_1) = g^{-1}(x_1)$ and $f(x_2) = g^{-1}(x_2)$. Since $g^{-1}(x)$ is monotonically increasing, we have $g^{-1}(x_1) \leqslant g^{-1}(x_2)$, which implies $f(x_1) \leqslant f(x_2)$. Meanwhile, since $f(x)$ is monotonically decreasing, $f(x_1) \geqslant f(x_2)$. Thus, we have $f(x_1) = f(x_2)$, and by monotonicity, $x_1 = x_2$. In other words, if the two functions intersect, there must be a unique intersection.

Since $g^{-1}(x)$ is always monotonically increasing and the existence of multistability requires the existence of multiple intersections between $g^{-1}(x)$ and $f(x)$, a monotonically decreasing $f(x)$ implies that the system cannot be multistable. In other words, if the system is multistable, then $f(x)$ cannot be monotonically decreasing. □

This result highlights the importance of self-excitation w_{EE} in equation S20 and equation S23—multistability can only occur when w_{EE} is sufficiently large. Correspondingly in the numerical result (Figure S1), the region of multistability appears only for larger w_{EE}'s.

Note that the above argument is not restricted to the present model, but applicable to models that share the geometry form of the Wilson-Cowan model in general. Nevertheless, one would hope to know how large a w_{EE} is large enough for multistability to be possible, and this depends on the specific formulation of the transfer function (equation 3) and the underlying assumptions about neuronal level properties (equation S8). Ideally, to know the minimal w_{EE}, one need to find the minimal slope of $H_E^{-1}(u(S_E))$ with respective to S_E, where $u(S_E) := S_E / (\tau_E \gamma_E (1 - S_E))$. The exact solution is, however, rather perplexing to calculate. Here we provide a

rough, but simple, estimation instead. The slope of interest is

$$\frac{\mathrm{d}}{\mathrm{d}\,S_E} H_E^{-1}(u(S_E)) = \frac{\mathrm{d}\,H_E^{-1}(u)}{\mathrm{d}\,u}\frac{\mathrm{d}\,u}{\mathrm{d}\,S_E} \tag{S24}$$

$$= \frac{\left(H_E^{-1}\right)'(u)}{\tau_E \gamma_E (1-S_E)^2}. \tag{S25}$$

Instead of finding the minimum of equation S25, we aim to find a representative point S_E^* such that equation S25 is relatively small.

One option is to use the minimum of the numerator. The minimum of the numerator $\left(H_E^{-1}\right)'(u)$ is simply the reciprocal of the maximum of $H_E'(v)$, where $v = H_E^{-1}(u)$. By design, H_E reaches its maximum slope a_E at the inflection point $\hat{x}$, where $H_E(v) = r_{max}/2$. That is, we need

$$\frac{S_E^*}{\tau_E \gamma_E (1-S_E^*)} = \frac{r_{max}}{2}$$

$$S_E^* = \frac{1}{2\, r_{max}^{-1} \tau_E^{-1} \gamma_E^{-1} + 1}.$$

But note here that, in the case where r_{max} is a large number, the representative point S_E^* is very close to one, which further results in a small denominator in equation S25 and a large slope for H_E^{-1}. Thus, the inflection point of $H_E(v)$ is not a very good choice.

To avoid the small denominator problem for equation S25, we need to choose a S_E^* as small as possible while $H_E(v)$ remains close to the line $a_E\, v - b_E$. For this purpose, we take v^* to be the intersection between the line $a_E\, v - b_E$ and the horizontal axis,

$$\begin{aligned} & a_E\, v^* - b_E = 0 \\ \Rightarrow\, & v^* = \frac{b_E}{a_E} \\ \Rightarrow\, & H_E(v^*) \approx \frac{1}{d_E}, \quad H_E'(v^*) \approx \frac{a_E}{2} \end{aligned} \tag{S26}$$

(approximate values can be obtained from the Taylor expansion of $\hat{H}_E$ near v^*). Given equation S26, we need

$$\frac{S_E^*}{\tau_E \gamma_E (1-S_E^*)} = \frac{1}{d_E} \tag{S27}$$

$$\Rightarrow S_E^* = \frac{1}{d_E \tau_E^{-1} \gamma_E^{-1} + 1} \tag{S28}$$

and

$$\left.\frac{\mathrm{d}\,H_E^{-1}(u(S_E))}{\mathrm{d}\,S_E}\right|_{S_E = S_E^*} = \frac{2}{a_E \tau_E \gamma_E (1-S_E^*)^2}$$

$$= \frac{2(1 + d_E^{-1}\tau_E\gamma_E)^2}{a_E \tau_E \gamma_E} =: h_E. \tag{S29}$$

Now for the nullcline $S_I = f(S_E)$ to have a positive slope at S_E^*, one simply needs

$$w_{EE} > h_E. \tag{S30}$$

Here h_E is approximately 0.2 based on the present parameter choices, inherited from Wong and Wang's initial derivation [5]. This result is confirmed numerically by the bifurcation diagrams (Figure 4a-c vs. Figure S5a) of the local model—multistability exists for some level of input I_E when $w_{EE} > 0.2$.

Oscillation. Now we look for the conditions for oscillation to emerge. Here we are mainly concerned with the oscillation occurring on the ascending segment of $S_I = f(S_E)$ (red nullcline). Following a similar argument as Wilson and Cowan [2], one notice that for the flow around a fixed point—an intersection between the nullclines—to have consistent rotation, the nullcline $g^{-1}(S_E)$ (blue) must have a greater slope than $f(S_E)$ (red nullcline). Qualitatively, one would expect oscillation to be induced by increasing w_{EI}, which twists $g(S_I)$ (blue nullcline) counterclockwise. This expectation is confirmed by the numerical results in Figure S1a-d: oscillation emerges for sufficiently large w_{EI} for fixed points on the ascending branch of $S_I = f(S_E)$ (Figure S2a-d).

Quantitatively, we consider the derivative of the two nullclines at a respective representative point. First, we extend the results in equation S28-S29 to the second nullcline $S_E = g(S_I)$ (blue):

$$S_I^* = \frac{1}{d_I \tau_I^{-1} \gamma_I^{-1} + 1} \tag{S31}$$

$$h_I := \left. \frac{\mathrm{d}\, H_I^{-1}(u(S_I))}{\mathrm{d}\, S_I} \right|_{S_I = S_I^*} = \frac{2(1 + d_I^{-1} \tau_I \gamma_I)^2}{a_I \tau_I \gamma_I}. \tag{S32}$$

For parameters used in the present study, $h_I \approx 0.4$. We have the slope of the two nullclines at their respective representative points,

$$f'(S_E^*) = \frac{w_{EE} - h_E}{w_{IE}} \tag{S33}$$

$$g'(S_I^*) = \frac{w_{II} + h_I}{w_{EI}}, \tag{S34}$$

and we need

$$\frac{1}{g'(S_I^*)} > f'(S_E^*) \tag{S35}$$

$$\Rightarrow \frac{w_{EI}}{w_{II} + h_I} > \frac{w_{EE} - h_E}{w_{IE}}$$

$$\Rightarrow w_{EI} > \frac{(w_{EE} - h_E)(w_{II} + h_I)}{w_{IE}}. \tag{S36}$$

With balanced inhibitory feedback $w_{IE} = w_{EE}$, we have

$$w_{EI} > (1 - h_E / w_{EE})(w_{II} + h_I). \tag{S37}$$

For very large w_{EE}, one simply need

$$w_{EI} > w_{II} + h_I. \tag{S38}$$

Given the present parameter choices, we need $w_{EI} > 0.45$ to induce oscillation for some level of input I_E and I_I. This is in line with the numerical results in Figure S1. For $h_E > 0$, as assumed here, lowering w_{EE} also lowers the threshold for oscillation.

Linear stability analysis. In addition to the presence of oscillation, one would also want to know if such oscillation is sustainable or damped. Here we extend the above analysis by linearizing the system near a specific fixed point. A fixed point is where the two nullclines (equations S20-S21) intersect. Conveniently, we let them intersect at their respective representative points $(S_E^*, f(S_E^*))$ and $(g(S_I^*), S_I^*)$ (see equation S28 and equation S31),

$$S_E^* = g(S_I^*) \tag{S39}$$

$$f(S_E^*) = S_I^*. \tag{S40}$$

The two equations can be satisfied by the appropriate choice of I_E and I_I. The fixed point of our choice (S_E^*, S_I^*) inherits a couple of properties from the above analysis, which we shall soon see. First, we define

$$\frac{\mathrm{d}\, S_E}{\mathrm{d}\, t} = F(S_E, S_I) := -\frac{S_E}{\tau_E} + (1 - S_E)\gamma_E\, H_E(w_{EE}S_E - w_{IE}S_I + I_E) \tag{S41}$$

$$\frac{\mathrm{d}\, S_I}{\mathrm{d}\, t} = G(S_E, S_I) := -\frac{S_I}{\tau_I} + (1 - S_I)\gamma_I\, H_I(w_{EI}S_E - w_{II}S_I + I_I). \tag{S42}$$

At the fixed points, we have from equation S41

$$H_E(w_{EE}S_E^* - w_{IE}S_I^* + I_E) = \frac{S_E^*}{\tau_E\gamma_E(1 - S_E^*)} \tag{S43}$$

$$= \frac{1}{d_E} \quad \text{(by definition, c.f. equation S27)} \tag{S44}$$

which implies that

$$I_E = \frac{b_E}{a_E} - w_{EE}S_E^* + w_{IE}S_I^* \tag{S45}$$

and

$$H_E'(w_{EE}S_E^* - w_{IE}S_I^* + I_E) = \frac{a_E}{2} \quad \text{(per equation S26).} \tag{S46}$$

Similarly from equation S42, we have

$$H_I(w_{EI}S_E^* - w_{II}S_I^* + I_I) = \frac{S_I^*}{\tau_I\gamma_I(1 - S_I^*)} = \frac{1}{d_I} \tag{S47}$$

$$I_I = \frac{b_I}{a_I} - w_{EI}S_E^* + w_{II}S_I^* \tag{S48}$$

$$H_I'(w_{EI}S_E^* - w_{II}S_I^* + I_I) = \frac{a_I}{2}. \tag{S49}$$

Now we are take the partial derivatives of F and G at (S_E^*, S_I^*),

$$\left.\frac{\partial F}{\partial S_E}\right|_{(S_E^*, S_I^*)} = -\frac{1}{\tau_E} - \gamma_E H_E(w_{EE}S_E^* - w_{IE}S_I^* + I_E)$$
$$+ (1 - S_E^*)\gamma_E w_{EE} H_E'(w_{EE}S_E^* - w_{IE}S_I^* + I_E)$$
$$= -\frac{1}{\tau_E} - \frac{\gamma_E}{d_E} + w_{EE}\gamma_E a_E(1 - S_E^*)/2 \tag{S50}$$

$$\left.\frac{\partial F}{\partial S_I}\right|_{(S_E^*, S_I^*)} = -(1 - S_I^*)w_{IE}\gamma_E H_E'(w_{EE}S_E^* - w_{IE}S_I^* + I_E)$$
$$= -w_{IE}\gamma_E a_E(1 - S_I^*)/2 \tag{S51}$$

$$\left.\frac{\partial G}{\partial S_E}\right|_{(S_E^*, S_I^*)} = (1 - S_I^*)w_{EI}\gamma_I H_I'(w_{EI}S_E^* - w_{II}S_I^* + I_I)$$
$$= w_{EI}\gamma_I a_I(1 - S_I^*)/2 \tag{S52}$$

$$\left.\frac{\partial G}{\partial S_I}\right|_{(S_E^*, S_I^*)} = -\frac{1}{\tau_I} - \gamma_I H_I(w_{EI}S_E^* - w_{II}S_I^* + I_I)$$
$$- (1 - S_I)w_{II}\gamma_I H_I'(w_{EI}S_E^* - w_{II}S_I^* + I_I)$$
$$= -\frac{1}{\tau_I} - \frac{\gamma_I}{d_I} - w_{II}\gamma_I a_I(1 - S_I^*)/2. \tag{S53}$$

For simplicity, let parameters

$$\alpha_p := \frac{1}{\tau_p} + \frac{\gamma_p}{d_p} \tag{S54}$$

$$\beta_p := \gamma_p a_p (1 - S_p^*)/2 \tag{S55}$$

$$= \frac{\gamma_p a_p d_p}{2(d_p + \gamma_p \tau_p)} \tag{S56}$$

for $p \in \{E, I\}$. Note that by definition, both α_p and β_p are positive. Given parameters used in the present study, we have $\alpha_E \approx 14$, $\alpha_I \approx 111$, $\beta_E \approx 71$, and $\beta_I \approx 276$.

We write the Jacobian matrix as

$$\mathbf{J} = \begin{pmatrix} -\alpha_E + \beta_E w_{EE} & -\beta_E w_{IE} \\ \beta_I w_{EI} & -\alpha_I - \beta_I w_{II} \end{pmatrix}. \tag{S57}$$

The eigenvalues of the Jacobian are

$$\lambda_{1,2} = \frac{\operatorname{tr} \mathbf{J} \pm \sqrt{\operatorname{tr}^2 \mathbf{J} - 4 \det \mathbf{J}}}{2} \tag{S58}$$

where

$$\operatorname{tr} \mathbf{J} = -\alpha_E - \alpha_I + \beta_E w_{EE} - \beta_I w_{II} \tag{S59}$$

$$\det \mathbf{J} = \alpha_E \alpha_I + \alpha_E \beta_I w_{II} - \alpha_I \beta_E w_{EE} + \beta_I \beta_E (w_{IE} w_{EI} - w_{EE} w_{II}). \tag{S60}$$

Assuming that the system is already oscillatory near the fixed point, i.e. $\operatorname{tr}^2 \mathbf{J} < 4 \det \mathbf{J}$, to have sustained oscillation (limit cycle), we need

$$\begin{aligned} &\operatorname{tr} \mathbf{J} > 0 \\ \Rightarrow\ &w_{EE} > (\alpha_E + \alpha_I + \beta_I w_{II})/\beta_E. \end{aligned} \tag{S61}$$

Given the parameters used in the present study, the emergence of limit cycles requires $w_{EE} > 2$. Correspondingly in the numerical results (Figure S1), equation S61 provides an estimate of the lower bound of the Hopf bifurcation (gray dashed line). Note that stronger inhibitory-to-inhibitory connection w_{II} increases the minimal w_{EE} required to induce sustained oscillation. Overall, these analyses show that sustained oscillation requires both strong self-excitation and a sufficiently active inhibitory population.

In summary, we have shown analytically how structural connectivity w_{EE} and w_{EI} critically shape the dynamics—in this very low-dimensional parameter space, the system can easily switch between qualitatively different behavior. In particular, excitatory-to-inhibitory connectivity w_{EI} controls the emergence of oscillation; excitatory-to-excitatory connectivity w_{EE} controls both the emergence of multistability and sustained oscillation. The qualitative description of the system only depends on the gross geometric form of the Wilson-Cowan model, but the exact boundaries between regimes depend on the specific transfer function and the associated biophysical constraints.

S9 Analysis of the global model

Now we take a look at the deterministic version of the global model,

$$\frac{\mathrm{d}\, S_E^{(i)}}{\mathrm{d}\, t} = -\frac{S_E^{(i)}}{\tau_E} + (1 - S_E^{(i)}) \gamma_E H_E \left(w_{EE}^{(i)} S_E^{(i)} - w_{IE}^{(i)} S_I^{(i)} + I_G^{(i)}(\vec{S}_E) \right) \tag{S62}$$

$$\frac{\mathrm{d}\, S_I^{(i)}}{\mathrm{d}\, t} = -\frac{S_I^{(i)}}{\tau_I} + (1 - S_I^{(i)}) \gamma_I H_I \left(w_{EI}^{(i)} S_E^{(i)} - w_{II}^{(i)} S_I^{(i)} + I_I \right) \tag{S63}$$

where

$$I_G^{(i)}(\vec{S}_E) = G\sum_{\substack{j=1\\ j\neq i}}^{N} C_{ij} S_E^{(j)}. \tag{S64}$$

In this case, the nullclines are hyper-surfaces,

$$w_{IE}^{(i)} S_I^{(i)} = f^{(i)}\left(\vec{S}_E\right) := w_{EE}^{(i)} S_E^{(i)} - H_E^{-1}\left(\frac{S_E^{(i)}}{\tau_E \gamma_E (1 - S_E^{(i)})}\right) + G\sum_{j\neq i} C_{ij} S_E^{(j)} \tag{S65}$$

$$w_{EI}^{(i)} S_E^{(i)} = g^{(i)}\left(S_I^{(i)}\right) := w_{II}^{(i)} S_I^{(i)} + H_I^{-1}\left(\frac{S_I^{(i)}}{\tau_I \gamma_I (1 - S_I^{(i)})}\right) - I_I. \tag{S66}$$

From equation S65 one can see that the local effect of global coupling is simply tilting the nullcline $S_I^{(i)} = f^{(i)}\left(\vec{S}_E\right)/w_{IE}^{(i)}$ upwards with respect to $S_E^{(j)}$.

The tilting of the nullcline $S_I^{(i)} = f^{(i)}\left(\vec{S}_E\right)/w_{IE}^{(i)}$ impact its number of intersections with $S_E^{(i)} = g^{(i)}\left(S_I^{(i)}\right)/w_{EI}^{(i)}$ in each level set of $G\sum_{j\neq i} C_{ij} S_E^{(j)}$. The number of intersections consequently constrains the number of stable states. A precise characterization of intersections is beyond the scope of the present work. Nevertheless, we hope to provide a few insights about the global geometry below.

Multistability. Following a similar argument as for the local model, we first show that, without global interaction (i.e. $G = 0$), the system cannot be multistable, if w_{EE} is sufficiently small such that $f^{(i)}(\vec{S}_E)$ monotonically decreases with $S_E^{(i)}$ for all i. As shown above, the monotonicity condition implies that each local node by itself is not multistable.

Proof. Assume there are at least two distinct fixed points of the system: $\vec{S}^*$ and $\vec{S}^{**}$, where $\vec{S} = (\vec{S}_E, \vec{S}_I)$ and $\vec{S}_p = (S_p^{(1)}, \cdots S_p^{(i)}, \cdots S_p^{(N)})$ for $p \in \{E, I\}$. Since they are distinct points, there exists an $0 < i \leqslant N$ such that $S_E^{*(i)} \neq S_E^{**(i)}$ ($S_I^{*(i)} \neq S_I^{**(i)}$ implies $S_E^{*(i)} \neq S_E^{**(i)}$ due to the monotonicity of g). Without loss of generality, we let $S_E^{*(i)} < S_E^{**(i)}$.

Since we know that $g^{-1\,(i)}(w_{EI}^{(i)} S_E^{(i)})$ is always a monotonically increasing function, we have

$$g^{-1\,(i)}(w_{EI}^{(i)} S_E^{*(i)}) < g^{-1\,(i)}(w_{EI}^{(i)} S_E^{**(i)}) \tag{S67}$$

$$\Rightarrow S_I^{*(i)} < S_I^{**(i)}, \tag{S68}$$

which also implies that

$$f^{(i)}\left(\vec{S}_E^*\right) < f^{(i)}\left(\vec{S}_E^{**}\right) \tag{S69}$$

by definition of the nullcline $S_I^{(i)} = f^{(i)}\left(\vec{S}_E\right)/w_{IE}^{(i)}$, for any choice of G and C_{ij}.

Now if $f^{(i)}(\vec{S}_E)$ is monotonically decreasing with respect to $S_E^{(i)}$, we know that at least for $G = 0$,

$$f^{(i)}\left(\vec{S}_E^*\right) > f^{(i)}\left(\vec{S}_E^{**}\right), \tag{S70}$$

which leads to a contradiction. Thus, if the system has multiple fixed points, $f^{(i)}(\vec{S}_E)$ cannot be monotonically decreasing with respect to $S_E^{(i)}$ for all i when $G = 0$. □

However, given a sufficiently large global coupling, especially for $G > 1$, multistability becomes possible.

Proof. Following the above proof, the assumption $S_E^{*(i)} < S_E^{**(i)}$ leads us to equation S69, or $\Delta_G < 0$, where

$$\Delta_G := f_G^{(i)}\left(\vec{S}_E^{*}\right) - f_G^{(i)}\left(\vec{S}_E^{**}\right) \tag{S71}$$

for any global coupling $G \geqslant 0$.

On the other hand, for the special case of $G = 0$, we can plug equation S65 into the definition S71 and have

$$\Delta_0 = f_{G=0}^{(i)}\left(\vec{S}_E^{*}\right) - f_{G=0}^{(i)}\left(\vec{S}_E^{**}\right) = w_{IE}^{(i)}\left(S_I^{*(i)} - S_I^{**(i)}\right) \tag{S72}$$

$$= f_{G=0}^{(i)}\left(S_E^{*(i)}\right) - f_{G=0}^{(i)}\left(S_E^{**(i)}\right) > 0, \tag{S73}$$

by our assumption that $f_G^{(i)}(\vec{S}_E)$ is a monotonically decreasing function with respect to $S_E^{(i)}$. Since by definition, the coordinates of each fixed point is bounded between 0 and 1, we have

$$0 < \Delta_0 \leqslant w_{IE}^{(i)}. \tag{S74}$$

In the case of $G = 0$, this leads to a contradiction $\Delta_G > 0$, as we have already shown above.

Now we consider what happens when $G > 0$. Again, by plugging equation S65 into the definition S71, we have

$$\begin{aligned}\Delta_G &= \Delta_0 + G\sum_{j\neq i} C_{ij}S_E^{*(j)} - G\sum_{j\neq i} C_{ij}S_E^{**(j)} \\ &= \Delta_0 + G\sum_{j\neq i} C_{ij}(S_E^{*(j)} - S_E^{**(j)}).\end{aligned} \tag{S75}$$

We need a bound on the second term in equation S75. Since $G > 0$ and $C_{ij} \geqslant 0$,

$$\begin{aligned}\left|G\sum_{j\neq i} C_{ij}(S_E^{*(j)} - S_E^{**(j)})\right| &\leqslant G\sum_{j\neq i} C_{ij}\left|(S_E^{*(j)} - S_E^{**(j)})\right| \\ &\leqslant G\sum_{j\neq i} C_{ij} && \text{(since } 0 \leqslant S_E^{(j)} \leqslant 1\text{)} \\ &\leqslant G && \text{(by equation 7).}\end{aligned}$$

This gives us

$$\Delta_0 - G \leqslant \Delta_G \leqslant \Delta_0 + G. \tag{S76}$$

Thus, contradiction with equation S69 is inevitable if $G < \Delta_0$. On the other hand, by equation S74, we know that for $G > \Delta_0$, there exists some $\vec{S}_E^{*}$ and $\vec{S}_E^{**}$ for some global network C_{ij} such that $\Delta_G < 0$ consistent with equation S69. Thus it is possible for the global model to be multistable if $G > \Delta_0$, especially if $G > w_{IE}^{(i)}$, or $G > w_{EE}^{(i)}$ given matched inhibitory feedback $w_{EE} = w_{IE}$. This does not mean, however, that the system has to be multistable, due to the dependency on C_{ij}. □

To summarize, the above analyses suggest that a collection of brain regions that have no independent memory capacity (i.e. multistability) can *acquire* memory capacity when connected to each other in a global network, given sufficient global coupling. We further support this claim with numerical analysis (Figure S5). We refer to this kind of memory as *synergistic* memory—it is an emergent property that the parts themselves do not possess.

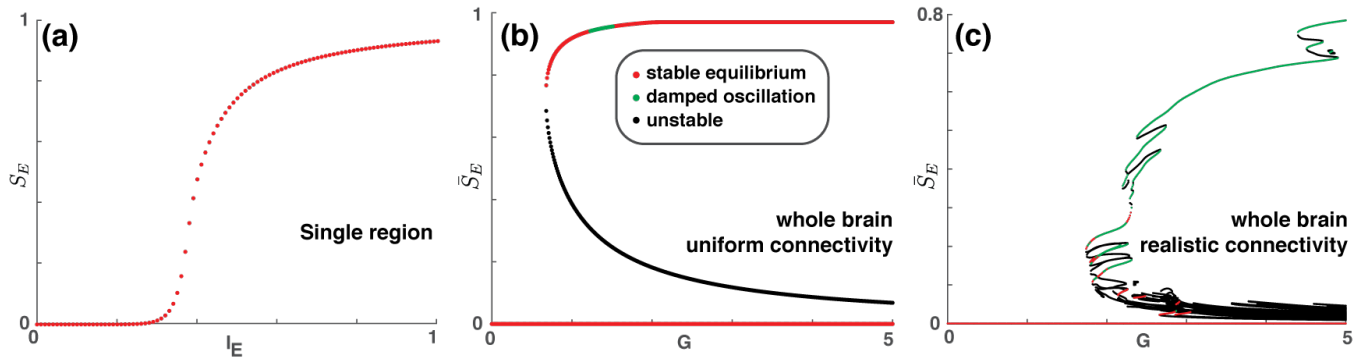

Figure S5: **Synergistic memory between monostable nodes**. Three bifurcation diagrams are shown for local parameters $w_{EE} = 0.1$ and $w_{EI} = 0.35$. They correspond to Figure 4a, d, g but with a lower w_{EE} such that each local node by itself is monostable for any level of input (a). While each local node is completely monostable (no memory capacity), once there is sufficient global coupling G between them, the whole brain acquires memory capacity (b, c) that cannot be attributed to the parts alone—synergistic memory. Nevertheless, the size of the global memory capacity is still fundamentally constrained by the complexity of the local node (42 attractor branches in (c), very small compare to Figure 4g, h, i). See text for further discussion.

What we have not addressed in the above analyses is to what extent the global system is multistable—what is the number of stable states, or the size of the memory capacity—and what are the contributions from local self-excitation and global network connectivity. An analytical approach to this problem is difficult; thus, it is mainly addressed numerically (c.f. Figure S5 and Figure 4). Nevertheless, we provide an intuitive argument below as to how local and global connectivity affects the relevant geometrical properties of the dynamical system.

Local origin of geometrical complexity. At an intuitive level, the number of intersections between these hypersurfaces (equation S65-S66) is likely to increase with the number of folds of each surface. In the present case, the folding of hypersurfaces entails the temporary reversal of the sign of its partial derivative along a certain direction. Observe equation S65 and see that global coupling cannot create any folding of the surfaces. Thus, the geometrical complexity of the nullclines purely depends on the local properties of each node, in particular, the folding effect of self-excitation $w_{EE}^{(i)}$.

The effect of global coupling. Without global coupling ($G = 0$), the number of fixed points of the global model is simply

$$n = \prod_{i=1}^{N} n_0^{(i)} \leqslant \left(\max_i n_0^{(i)} \right)^N \tag{S77}$$

where $n_0^{(i)}$ is the number of fixed points for each corresponding local model when $I_E = 0$. Introducing global coupling ($G \neq 0$) tilts each surface (equation S65) in a way dependent on the structure connectivity C_{ij}. This may remove or introduce new intersections between the surfaces without changing the geometrical complexity of these surfaces. Thus, global coupling allows system-level multistability to be created synergistically, given appropriate structural connectivity C_{ij}.

In summary, local and global coupling produce different geometrical effects on the system and jointly affect the number of possible stable states.

References

1. Deco, G. *et al.* Resting-state functional connectivity emerges from structurally and dynamically shaped slow linear fluctuations. *Journal of Neuroscience* **33,** 11239–11252 (2013).
2. Wilson, H. R. & Cowan, J. D. Excitatory and inhibitory interactions in localized populations of model neurons. *Biophysical Journal* **12,** 1–24 (1972).
3. Wilson, H. R. & Cowan, J. D. A mathematical theory of the functional dynamics of cortical and thalamic nervous tissue. *Kybernetik* **13,** 55–80 (1973).
4. Wang, X.-J. Probabilistic decision making by slow reverberation in cortical circuits. *Neuron* **36,** 955–968 (2002).
5. Wong, K.-F. & Wang, X.-J. A recurrent network mechanism of time integration in perceptual decisions. *Journal of Neuroscience* **26,** 1314–1328 (2006).
6. Deco, G. *et al.* How local excitation–inhibition ratio impacts the whole brain dynamics. *Journal of Neuroscience* **34,** 7886–7898 (2014).
7. Demirtaş, M. *et al.* Hierarchical heterogeneity across human cortex shapes large-scale neural dynamics. *Neuron* **101,** 1181–1194.e13 (2019).
8. Renart, A., Brunel, N. & Wang, X.-J. in *Computational Neuroscience: A Comprehensive Approach* (ed Feng, J.) 432–490 (CRC Press, 2003).
9. Brunel, N. & Wang, X.-J. Effects of neuromodulation in a cortical network model of object working memory dominated by recurrent inhibition. *Journal of Computational Neuroscience* **11,** 63–85 (2001).
10. Abbott, L. F. & Chance, F. S. Drivers and modulators from push-pull and balanced synaptic input. *Progress in Brain Research* **149,** 147–155 (2005).
11. Buxton, R. B., Wong, E. C. & Frank, L. R. Dynamics of blood flow and oxygenation changes during brain activation: The balloon model. *Magnetic Resonance in Medicine* **39,** 855–864 (1998).
12. Mandeville, J. B. *et al.* Evidence of a Cerebrovascular Postarteriole Windkessel with Delayed Compliance. *Journal of Cerebral Blood Flow & Metabolism* **19,** 679–689 (1998).
13. Friston, K., Mechelli, A., Turner, R. & Price, C. Nonlinear responses in fMRI: the Balloon model, Volterra kernels, and other hemodynamics. *NeuroImage* **12** (2000).
14. Friston, K., Harrison, L. & Penny, W. Dynamic causal modelling. *NeuroImage* **19,** 1273–1302 (2003).
15. Welch, P. The use of fast Fourier transform for the estimation of power spectra: A method based on time averaging over short, modified periodograms. *IEEE Transactions on Audio and Electroacoustics* **15,** 70–73 (1967).
16. Van Essen, D. C. *et al.* The WU-Minn Human Connectome Project: An overview. *NeuroImage* **80,** 62–79 (2013).